Electronic Transport in Graphene

Yuanbo Zhang

Advisor: Philip Kim

Submitted in partial fulfillment of the
requirements for the degree
of Doctor of Philosophy
in the Graduate School of Arts and Sciences

COLUMBIA UNIVERSITY

2006

ABSTRACT

Electronic Transport in Graphene

Yuanbo Zhang

This dissertation focuses on the electronic transport properties of graphene, a single atomic layer of graphite. Graphene is a novel two-dimensional system in which electron transport is effectively governed by the relativistic quantum theory. We discover a variety of new phenomenon which stem from the "relativistic" nature of the electron dynamics in graphene.

An unusual quantum Hall (QH) effect is discovered in graphene at low temperatures and strong magnetic fields. Unlike conventional two-dimensional electron systems, in graphene the observed quantization condition is characterized by half integers rather than integers. Our investigation of the magneto-oscillations in resistance reveals a Berry's phase of π associated with the electron motion in graphene. The half-integer quantization, as well as the Berry's phase, is attributed to the peculiar topology of the graphene band structure with a linear dispersion relation and vanishing mass near the Dirac point, which can be described by relativistic quantum electrodynamics. This is further confirmed by our measurement of the effective carrier mass, m^*, which obeys Einstein's equation: $E = m^* c_*^2$ where $c_* \approx c/300$ is the effective speed of light for electrons in graphene.

The availability of high magnetic fields up to 45 Tesla allows us to study the

magneto-transport in graphene in the extreme quantum limit. Under such condition, we discover new sets of QH states at filling factors $\nu = 0, \pm 1, \pm 4$, indicating the lifting of the four-fold degeneracy of the previously observed QH states at $\nu = \pm 4(|n|+1/2)$, where n is the Landau level index. In particular, the presence of the $\nu = 0, \pm 1$ QH states indicates that the Landau level at the charge neutral Dirac point splits into four sub-levels, lifting both sublattice and spin degeneracy, thereby potentially indicating a many-body correlation in this LL. The QH effect at $\nu = \pm 4$ is investigated in tilted magnetic fields and is attributed to lifting of the $n = \pm 1$ spin-degeneracy of the Landau level.

We devote one chapter to the investigation of multi-layer graphene. Strong conductance modulation as a function of gate voltage is observed in the thin crystallite devices (thickness $\sim$ 12 nm). The temperature-dependent resistivity data are analyzed in the frame work of the simple two-band (STB) model. They indicate more boundary scattering contribution in the thinner graphite samples. Galvanomagnetic transport study those samples shows strong modulation of the Hall resistance as well as the magneto-resistance, a phenomena that was not observed before in the bulk, has been observed as the applied gate voltage changes. The Landau level formation of electron and hole carriers is also tuned by the gate. The observed phenomenon can be well described by the STB model, taking into account the carrier density gradient induced by the gate electrode. By fitting the temperature damping of the magneto-resistance oscillations, we obtain the effective carrier masses in the mesoscopic graphite samples.

Contents

List of Figures

Acknowledgments

I am most indebted to my advisor Professor Philip Kim for his patient guidance and constant support. Working is his group was truly a wonderful experience filled with exciting experiments and inspirational discussions. His dedication and passion for doing science was a constant source of enthusiasm for me, and will keep me going for the years to come.

Very special thanks to Professor Horst Stormer. He is a great person to work with and to learn from. I enjoyed the enlightening discussions with him, and was always amazed by his insights.

I would also like to thank Professors Aron Pinczuk, Tony Heinz, and Igor Aleiner for making time to be in my dissertation committee.

Part of the experiment in this dissertation was done, in a very productive collaboration with Dr. Zhigang Jiang, in National High Magnetic Field Laboratory in Tallahassee, Florida. The Laboratory is a fantastic place to do physics. Data taking during late or early hours would have been impossible without Zhigang's instrumentation expertise and amazing energy. Thanks to him for driving me between the condo and the lab, and for the lively discussions inside the work and out in the fast-food restaurants. The people at the facility are true professionals. They have been important for smooth experiments for the outside users. I am particularly grateful to

Ms. Merry-Ann Johnson, Messrs. Bobby-Joe Pullum, Gordon Armstrong, and Drs. Bruce Brandt, Scott Hannahs, Eric Palm, Stan Tozer Tim Murphy.

During my first two years at Columbia, I was fortunate to have the opportunity to try my hands on particle physics, with the support of Professors Allen Caldwell and Frank Sciulli. Working at DESY, Hamburg was a peaceful and pleasant experience which I will never forget.

The friendly help and support of faculty and staff members of the Department of Physics makes life for the students. I am grateful to Professor Andrew Millis, Allan Blaer, Tony Heinz, Ms. Lalla Grimes, Myrna Tengco, Nicole Griggs, Giuseppina Cambareriand, Partricia Fuentes, Mr. John Carr III. for their help over the years.

My fellow group memebers have been terrific. Working with Drs. Joshua Small, Barbaros Oezyilmaz, Byung Hee Hong, Messrs. Meninder Purewal, Yuri Zuev and Ms. Melinda Han , Ju Young Lee has been a lot of fun. I have learned a lot from each of them.

Previous generation of students and postdocs are an interesting and joyful bunch. Their usual gathering places are 9th floor Schapiro and many terrific restaurants previously unknown to me. I am grateful that they always took me along. These people are Drs. Jun Zhu, Cyrus Hirjibehedin, Syum Shyed, Irene Dujovne, Feng Wang, Aditi Mitra, Etienne De Poortere, Jochen Ulrich, Daniel Quinn and Hayn Park.

I am very lucky to have Ms. Yan-Wen Tan with me for the past six years at Columbia. During these years, she has always been my best friend with love and support. I couldn't imagine going all the way for this Ph.D. without her. A large portion of this Ph.D. has to be credited to her, although she is going to get her own very soon. Our wedding is scheduled next week on August 25th, 2006, and our life

together is just about to get started.

My family has been a constant source of encouragement. In a remote place called United States, their love and support make me strong. Thank you, mom and dad, for your understanding and encouragement over the years. I hope this Ph.D. will bring you some joy.

During the final preparation of this dissertation, my grandma and grandpa past away. I always remember that grandpa and I worked together on the vegetable fields in his backyard and I always remember what grandma told me about their difficult times during the Culture Revolution. I will remember them forever.

Chapter 1

Introduction

1.1 What is Graphene?

Graphene is single atomic sheet of carbon atoms that are arranged into a honeycomb lattice. It can be viewed as a giant two-dimensional (2D) fullerene molecule, an unrolled single wall carbon nanotube, or simply a single layer of lamellar graphite crystal. The crystal structure of graphene is shown in Fig. 1.1. The lattice vectors can be written as:

$$\mathbf{a_1} = a(1/2, \sqrt{3}/2) \qquad \mathbf{a_2} = a(-1/2, \sqrt{3}/2) \tag{1.1}$$

in the (x, y) coordinates with the lattice constant $a = \sqrt{3}a_0$. Here $a_0 = 1.4$ Å is the distance between the nearest neighbors. This set of lattice vectors correspond to a reciprocal lattice with the base vectors

$$\mathbf{b_1} = \frac{4\pi}{\sqrt{3}a}(\sqrt{3}/2, 1/2) \qquad \mathbf{b_2} = \frac{4\pi}{\sqrt{3}a}(-\sqrt{3}/2, 1/2) \tag{1.2}$$

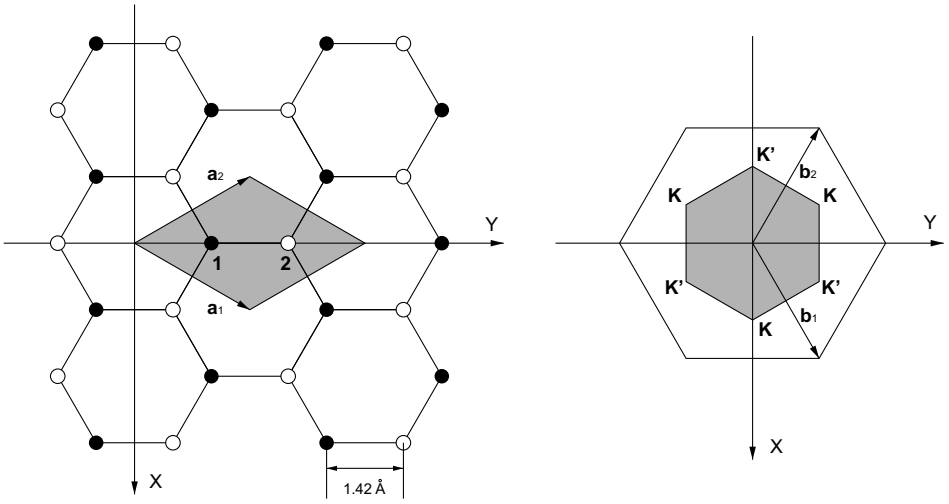

Figure 1.1: Graphene and its reciprocal lattice. Left: $\mathbf{a_1}$ and $\mathbf{a_2}$ are the lattice vectors. There are two carbon atoms (1 and 2) in one unit cell (shaded area). Right: the reciprocal lattice of graphene is defined by $\mathbf{b_1}$ and $\mathbf{b_2}$. The first Brillouin zone is shown as shaded hexagonal.

as shown in Fig. 1.1.

There are two carbon atoms in one unit cell. Every carbon atom has four valence electrons, of which three are used for the chemical bonds in the graphene plane. We refer them as σ bonds. The fourth electron is in a $2p_z$ orbital which is oriented perpendicular to the plane. Since the σ bonds are extremely localized and does not contribute to the electronic conduction, we are only concerned with the energy band structure of the fourth electron (We will refer it as π band). Note that there are two such electrons in one unit-cell, therefore there should be two π-bands, π and π^*, with π corresponding to valence band (bonding) and π^* corresponding to the conduction band (anti-bonding).

The band structure of graphene can be calculated using tight-banding method. This was first done by Wallace (1947) [1] (see [2] for an instructive introduction). We

start with the general form of the Bloch wave function:

$$\psi = \sum_{\mathbf{R}} e^{i\mathbf{k}\cdot\mathbf{R}}\phi(\mathbf{r}-\mathbf{R}) \tag{1.3}$$

where $\mathbf{R}$ is the set of lattice vectors defined by linear combinations of $\mathbf{a_1}$ and $\mathbf{a_2}$. $\phi(\mathbf{r})$ is the slow-varying envelope function to be calculated. In the framework of the the tight-binding method, we assume the atomic wave functions are well localized at the position of the atoms. When the overlap between neighboring atomic wave functions, though nonzero, is exceedingly small, ϕ can be approximated by a linear combination of a set of atomic wave functions. This is why the tight-binding method is sometimes known as the linear combination of atomic orbitals (LCAO). In the case of graphene, we consider only the $2p_z$ orbitals. There are two such orbitals per unit cell, which we shall call ϕ_1 and ϕ_2 with 1 and 2 referring to the two carbon atoms in one unit cell (Fig. 1.1). The total wave function can be written as

$$\phi = b_1\phi_1 + b_2\phi_2 \tag{1.4}$$

where b_1 and b_2 are constant and $|b_1|^2 + |b_2|^2 = 1$. We now consider a single electron which experiences the atomic potential given by all the carbon atoms. The Hamiltonian is

$$H = \frac{\nabla^2}{2m} + \sum_{\mathbf{R}} \left(V_{atom}(\mathbf{r}-\mathbf{r_1}-\mathbf{R}) + V_{atom}(\mathbf{r}-\mathbf{r_2}-\mathbf{R})\right) \tag{1.5}$$

where $\mathbf{r_1}$ and $\mathbf{r_2}$ are positions of the two atoms in the unit cell (Fig. 1.1). b_1 and b_2 can be obtained by solving the Shrodinger equation

$$H\psi = E\psi \tag{1.6}$$

We need two equations for two parameters (b_1 and b_2). This is done by projecting Eq. 1.6 onto the two states ϕ_1 and ϕ_2

$$\langle\phi_j|H|\psi\rangle = E\langle\phi_j|\psi\rangle \tag{1.7}$$

where $j = 1, 2$. Here we adopt the more compact bra and ket notation.

Let us first calculate $\langle\phi_j|\psi\rangle$ by plugging in Eq. 1.3. It is important to note that only the nearest neighbor products have to be taken into account. Therefore we only need to consider $\mathbf{R} = \mathbf{0}, \mathbf{a_1}, \mathbf{a_2}$ terms in $|\psi\rangle$. Two equations are obtained as a result

$$\langle\phi_1|\psi\rangle = b_1 + b_2\langle\phi_1|\phi_2\rangle(1 + e^{-i\mathbf{k}\cdot\mathbf{a_1}} + e^{-i\mathbf{k}\cdot\mathbf{a_2}}) \tag{1.8}$$

$$\langle\phi_2|\psi\rangle = b_2 + b_1\langle\phi_2|\phi_1\rangle(1 + e^{i\mathbf{k}\cdot\mathbf{a_1}} + e^{i\mathbf{k}\cdot\mathbf{a_2}}) \tag{1.9}$$

It is easy to see that $\langle\phi_1|\phi_2\rangle = \langle\phi_2|\phi_1\rangle$. We will assume that they are real, and denote them with γ_0.

We now turn to $\langle\phi_j|H|\psi\rangle$. We first note that the total Hamiltonian H contains the exact atomic Hamiltonian for atom 1, $H_1 = \frac{\nabla^2}{2m} + V_{atom}(\mathbf{r} - \mathbf{r_1})$, and the potential from all other atoms which we simply call ΔH_1. Likewise for atom 2. Therefore, we can write

$$H = H_1 + \Delta H_1 = H_2 + \Delta H_2 \tag{1.10}$$

Since ϕ_j are eigenfunctions of H_j, we have a simple relation

$$H_j|\phi_j\rangle = \epsilon_j|\phi_j\rangle \tag{1.11}$$

where ϵ_j is the energy of the carbon $2p_z$ orbital. Obviously, $\epsilon_1 = \epsilon_2$, so we sill simply call them ϵ_0. Furthermore, we are free to set the zero energy, so we chose $\epsilon_0 = 0$.

Now we have

$$\begin{aligned} \langle\phi_1|H|\psi\rangle &= \langle\phi_1|H_1 + \Delta H_1|\psi\rangle \\ &= \langle\phi_1|\Delta H_1|\psi\rangle \end{aligned} \tag{1.12}$$

$$\begin{aligned} \langle\phi_2|H|\psi\rangle &= \langle\phi_2|H_2 + \Delta H_2|\psi\rangle \\ &= \langle\phi_2|\Delta H_2|\psi\rangle \end{aligned} \tag{1.13}$$

Again, when calculating terms $\langle\phi_j|\Delta H_j|\psi\rangle$, only on-site and the nearest neighbor overlaps are relevant. After this consideration, there are only a few terms retained

$$\langle\phi_1|\Delta H_1|\psi\rangle = b_1\beta + b_2\gamma_1 f^*(\mathbf{k}) \tag{1.14}$$

$$\langle\phi_2|\Delta H_2|\psi\rangle = b_2\beta + b_1\gamma_1 f(\mathbf{k}) \tag{1.15}$$

Here we used the abbreviations

$$\beta = \langle\phi_1|\Delta H_1|\phi_1\rangle \tag{1.16}$$

$$\gamma_1 = \langle\phi_1|\Delta H_1|\phi_2\rangle = \langle\phi_2|\Delta H_2|\phi_1\rangle \tag{1.17}$$

$$f(\mathbf{k}) = 1 + e^{i\mathbf{k}\cdot\mathbf{a_1}} + e^{i\mathbf{k}\cdot\mathbf{a_2}} \tag{1.18}$$

Putting together Eq. 1.8 and 1.14, the Shrodinger equation 1.7 is transformed into an eigenvalue equation

$$\begin{pmatrix} \beta & f^*(\mathbf{k})(\gamma_1 - \gamma_0 E) \\ f(\mathbf{k})(\gamma_1 - \gamma_0 E) & \beta \end{pmatrix} \begin{pmatrix} b_1 \\ b_2 \end{pmatrix} = E \begin{pmatrix} b_1 \\ b_2 \end{pmatrix} \tag{1.19}$$

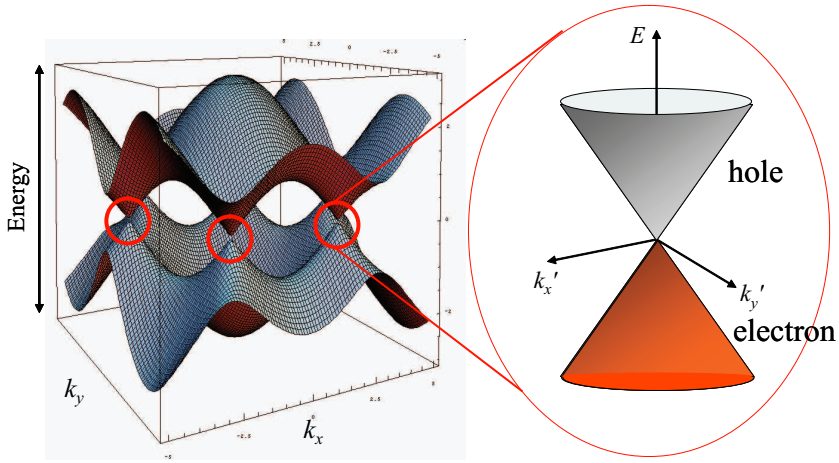

Figure 1.2: Energy band structure of graphene. The valence band (lower band) and conduction band (upper band) touch at six points, where the Fermi level is located. In the vicinity of these points, the energy dispersion relation is linear.

from which the dispersion relation $E = E(\mathbf{k})$ can be obtained. Note that by writing the Shrodinger equation this way, we assume the two basis wavefunctions: $\psi_{(1,2)} = \sum_{\mathbf{R}} e^{i\mathbf{k}\cdot\mathbf{R}}\phi_{(1,2)}(\mathbf{r}-\mathbf{R})$. β is the energy variation of the p_z atomic orbital induced by all the other carbon atoms in the graphene plane. It corresponds to a small rigid shift of the energy band, and can be neglected. Equation 1.19 is further simplified if we exploit the fact that γ_0 is small. Then the dispersion relation is simply

$$E(\mathbf{k}) = \pm\gamma_1|f(\mathbf{k})| \tag{1.20}$$

$$= \pm\gamma_1\sqrt{1+4\cos\left(\frac{k_y\sqrt{3}a}{2}\right)\cos\left(\frac{k_x a}{2}\right)+4\cos^2\left(\frac{k_x a}{2}\right)} \tag{1.21}$$

where k_x and k_y are the components of $\mathbf{k}$ in the (x, y) coordinates shown in Fig. 1.1.

The energy band structure (Eq. 1.20) is plotted in Fig. 1.2. Just as we discussed before, there are two bands: the valence band ($E < 0$) and the conduction band ($E > 0$). They touch at six points at the corners of the Brillouin zone, of which three

are equivalent (**K** points), and so are the other three (**K′** points). Since each carbon atom contributes one electron, the conduction band are completely filled up to those six points, where the Fermi level resides. For this reason, graphene is known as a zero-gap semiconductor/semimetal.

As far as the electronic transport is concerned, we are interested in the low energy region just around the $\mathbf{K}, \mathbf{K}'$ points. In this regime, the Hamiltonian can be approximated by its first order expansion. We first look at **K** point, around which we write $\mathbf{k} = \boldsymbol{\kappa} + \mathbf{K}$, and $E(\mathbf{k}) = \epsilon(\boldsymbol{\kappa}) + E(\mathbf{K})$. Expanding $f(\mathbf{k})$ to its first order, Eq. 1.19 reduces to

$$-\frac{\sqrt{3}\gamma_1 a}{2}\begin{pmatrix} 0 & \kappa_x - i\kappa_y \\ \kappa_x + i\kappa_y & 0 \end{pmatrix}\begin{pmatrix} b_1 \\ b_2 \end{pmatrix} = \epsilon(\boldsymbol{\kappa})\begin{pmatrix} b_1 \\ b_2 \end{pmatrix} \tag{1.22}$$

The dispersion relation then becomes very simple

$$\epsilon(\boldsymbol{\kappa}) = \mp\hbar v_F|\boldsymbol{\kappa}| \tag{1.23}$$

where v_F is the Fermi velocity given by the constant

$$v_F = \frac{\sqrt{3}\gamma_1 a}{2\hbar} \tag{1.24}$$

So the energy surface is two circular cones touching each other head to head (see Fig. 1.2). In these cones, the 2D energy spectrum is linear, and the electrons always move at a constant speed v_F. This is in perfect analogy to a relativistic massless particle, such as photons and massless neutrinos. Therefore the electron dynamics in graphene are effectively relativistic, where the speed of light is substituted by Fermi velocity v_F. Taking the known values for γ_1 (2.9 eV) and a (4.26 Å), v_F is estimated to be

$\approx 10^6$ m/s. So even through the carriers move at a speed much slower than the speed of light, it is remarkable to see that they behave as if they are relativistic particles with zero mass.

It is important to note that, even though we used a simple tight-binding model with only the nearest neighbors taken into account, the result (Eq. 1.23) is robust against any approximations regarding wavefunctions and is a result of the symmetry of graphene with spin-orbital coupling neglected [3].

Now written in a compact form, the Hamiltonian at **K** is

$$H = \hbar - v_F \widehat{\boldsymbol{\kappa}} \cdot \boldsymbol{\sigma} \tag{1.25}$$

Here we approximate the wave function with plane waves, and replace the wave number $\boldsymbol{\kappa}$ with operators $\widehat{\boldsymbol{\kappa}} = -i\nabla = -i(\widehat{x}\frac{\partial}{\partial x} + \widehat{y}\frac{\partial}{\partial y})$. $\boldsymbol{\sigma}$'s are the Pauli matrices, $\boldsymbol{\sigma} = \widehat{x}\sigma_x + \widehat{y}\sigma_y$. Eq. 1.25 is recognized as a 2D Dirac Hamiltonian for massless fermions with an extra minus sign. This Hamiltonian is well known for describing massless neutrinos in particle physics. As we shall discuss in the next section, the familiar concepts such as helicity can be readily recovered, and they have profound implications on the electronic transport properties of graphene.

1.2 Massless Dirac Fermion in Graphene

The states for the massless Dirac fermion Hamiltonian 1.25 is given by [3–6]:

$$|\boldsymbol{\kappa}\rangle = \frac{1}{\sqrt{2}} e^{i\boldsymbol{\kappa}\cdot\mathbf{r}} \begin{pmatrix} -ise^{-i\theta_\kappa/2} \\ e^{i\theta_\kappa/2} \end{pmatrix} \tag{1.26}$$

where θ_κ is the angle between $\boldsymbol{\kappa} = (\kappa_x, \kappa_y)$ and the y-axis (see Fig. 1.1), and $s = -1$ and $+1$ denote the states above and below **K**, respectively. The corresponding energy for these states is given by 1.23, and $s = -1/+1$ states have positive/negative energy respectively. The two components of the state vector give the amplitude of the electronic wave function on the atoms of the two sublattice, so the angle θ_κ determines the character of the underlying atomic orbital mixing.

The two-component vector in formula 1.26 can be viewed as a result of a spin-rotation of θ_κ from k_y axis, given by

$$R(\theta) = \exp\left(-i\frac{\theta}{2}\sigma_z\right) = \begin{pmatrix} e^{-i\theta/2} & 0 \\ 0 & e^{+i\theta/2} \end{pmatrix} \tag{1.27}$$

from $|s\rangle$, the eigenvector for the state with $\boldsymbol{\kappa}$ in the positive k_y direction (i.e. $\theta_\kappa = 0$)

$$|s\rangle = \frac{1}{\sqrt{2}} \begin{pmatrix} -is \\ 1 \end{pmatrix} \tag{1.28}$$

This rotation operation clearly resembles that of a two-component spinor describing the electron spin. Indeed, the above vector can be regarded as a pseudospin, arising from the symmetry of underlying honeycomb graphene lattice. The above operation also implies that the orientation of the pseudospin is tied to the $\boldsymbol{\kappa}$ vector. This is completely analogous to the real spin of a massless neutrino which always points along the propagation. For $s = +1$, i.e., the lower cone at **K** in Fig. 1.2, the states have pseudospin parallel to $\boldsymbol{\kappa}$, and thus correspond to right-handed neutrinos. For $s = -1$, i.e. the antiparticles in the upper cone, the situation is reversed, just like anti-neutrinos.

So far our analysis is focused on the **K** point. It would be interesting to see what

happens to the $\mathbf{K}'$ point. We apply a similar analysis to $\mathbf{K}'$, and the only difference is that now we expand the Hamiltonian in Eq. 1.19 around the $\mathbf{K}'$ point: $\mathbf{k} = \boldsymbol{\kappa} + \mathbf{K}'$, and $E(\mathbf{k}) = \epsilon(\boldsymbol{\kappa}) + E(\mathbf{K}')$. Instead of Eq. 1.22, we obtain a new equation

$$\frac{\sqrt{3}\gamma_1 a}{2} \begin{pmatrix} 0 & \kappa_x + i\kappa_y \\ \kappa_x - i\kappa_y & 0 \end{pmatrix} \begin{pmatrix} b_1 \\ b_2 \end{pmatrix} = \epsilon(\boldsymbol{\kappa}) \begin{pmatrix} b_1 \\ b_2 \end{pmatrix} \tag{1.29}$$

This leads to a Hamiltonian at $\mathbf{K}'$

$$H = \hbar v_F \widehat{\boldsymbol{\kappa}} \cdot \bar{\boldsymbol{\sigma}} \tag{1.30}$$

where $\bar{\boldsymbol{\sigma}}$ are the complex conjugate of the Pauli matrices $\boldsymbol{\sigma}$. This Hamiltonian is known to describe left-handed massless neutrinos. Therefore at $\mathbf{K}'$ the electron dynamics is again characterized by massless Dirac fermions, but with opposite helicity, as shown in Fig. 1.1.

The chirality of the electrons in graphene has important implications on the electronic transport in graphene. Following Ando et. al [5], let us consider a scattering process $\boldsymbol{\kappa} \rightarrow \boldsymbol{\kappa'}$ due to an potential $V(\mathbf{r})$ with a range larger than the lattice constant in graphene, so that it does not induce scattering between $\mathbf{K}$ and $\mathbf{K}'$ points. The resulting matrix element between these two states is given by [5, 6]

$$|\langle \boldsymbol{\kappa'}|V(\mathbf{r})|\boldsymbol{\kappa}\rangle|^2 = |V(\boldsymbol{\kappa} - \boldsymbol{\kappa'})|^2 \cos^2(\theta_{\kappa,\kappa'}/2) \tag{1.31}$$

where $\theta_{\kappa,\kappa'}$ is the angle between $\boldsymbol{\kappa}$ and $\boldsymbol{\kappa'}$, and the cosine term comes from the overlap of the initial and final spinors. A backscattering process corresponds to $\boldsymbol{\kappa} = -\boldsymbol{\kappa'}$. In this case, $\theta_{\kappa,\kappa'} = \pi$ and the matrix element vanishes. Therefore such backward scattering is completely suppressed. This is a direct consequence of the fact that an

electron in graphene, described by Eq. 1.25, has 'helicity', i.e. its pseudospin always points along its wave vector. The direction of the pseudospin is reversed in a backward scattering, leading to a destructive interference. The experimental significance of the Berry's phase of π is demonstrated by McEuen et al. [6] in single-wall carbon nanotubes (SWCNTs), which are essentially graphene rolled up into cylinders. The suppression of backscattering in metallic SWCNTs leads to a remarkably long electron mean free path in the order of micron.

The suppression of backward scattering can also be understood in terms of the Berry's phase induced by the pseudospin rotation. It has been demonstrated by Ando et. al [5] that a rotation in $\boldsymbol{\kappa}$ by 2π leads to a change of the phase of the wave function by π. The non-trivial Berry's phase may lead to non-trivial quantum correction, the so-called anti-localization, to the conductivity in graphene. Each scattering process corresponds to a complementary time-reversal process. In a conventional 2D electron system, the scattering amplitude and associated phase of each process and its complementary time-reversal process is equal. This constructive interference leads to the enhancement of the backward scattering amplitude and thus the localization of the electron states. This mechanism is known as weak localization. In graphene, however, each scattering process induces a rotation of the pseudospin, and results in a corresponding phase change of the wave function. This leads to a destructive interference for the backward scattering. Therefore the quantum correction to the conductivity in graphene should have a positive sign, which is yet to be observed experimentally.

However, the Berry's phase can be observed in the quantum oscillations induced by a uniform external magnetic field [7, 8]. In a semi-classical picture, the electrons orbit along a circle in $\mathbf{k}$ space when subjected to a magnetic field. The Berry's phase of π produced by the 2π rotation of the wave vector manifests itself as a phase shift of

the quantum oscillations, which will be the focus of the discussion of the next section.

1.3 Electron Dynamics in a Magnetic Field

1.3.1 Quantum Mechanical Description

Let us first consider the simplest case, a free electron moving in 2D subject to an perpendicular magnetic field, B. Classically, it goes around in a circular orbit with an angular frequency

$$\omega_c = eB/m \tag{1.32}$$

as a result of the Newton's Law: $md\mathbf{v}/dt = -e\mathbf{v}\times\mathbf{B}$. ω_c is called cyclotron frequency. The radius of the orbit is proportional to its velocity, $R_c = v/\omega_c$, and it changes continuously as B varies. Of course, this picture is modified in quantum mechanics, because first of all the motion of the electron has to be quantized.

A quantum mechanical treatment of the same problem starts with the following Hamiltonian

$$H = \frac{1}{2m}\left(\mathbf{P} + e\mathbf{A}\right)^2 \tag{1.33}$$

where $\mathbf{P}$ is the momentum operator $-i\hbar\bigtriangledown$ and $\mathbf{A}$ is the vector potential for the magnetic field. The solution to this problem is well know (see any quantum mechanics textbook, such as [9]). By choosing a Landau gauge, i.e. $\mathbf{A} = -By\widehat{x}$, the Shrodinger equation becomes

$$\left(\frac{P^2}{2m} - \frac{eB}{m}yP_x + \frac{1}{2}m\omega_c^2y^2\right)\psi = E\psi \tag{1.34}$$

where ω_c is cyclotron frequency defined previously. After separating the variables by assuming solutions having the form $\psi(x,y) = \exp(ikx)\chi_{n,k}(y)$, this equation is

the same as the one describing a harmonic oscillator and the eigenfunctions and eigenenergies are given by

$$\chi_{n,k}(y) = u_n(\eta - \eta_k) \tag{1.35}$$

$$E_n = \left(n + \frac{1}{2}\right)\hbar\omega_c, \quad n = 0, 1, 2, ... \tag{1.36}$$

where

$$u_n(\eta) = \exp(-\eta^2/2)H_n(\eta) \tag{1.37}$$

$$\eta = y\sqrt{m\omega_c/\hbar} \quad \text{and} \quad \eta_k = \sqrt{\hbar m\omega_c}k/eB \tag{1.38}$$

with $H_n(\eta)$ being the nth Hermite polynomial. The discreet energy levels are called Landau levels (LLs), and they are equally separated by the cyclotron energy $\hbar\omega_c$, which scales proportionally with the magnetic field. Note that even at the zeroth LL, there is a finite energy of $\hbar\omega_c/2$.

An inspection of the density of states (DOS) reveals that, in a magnetic field, the zero-field DOS characterized by a step function

$$N(E) = \frac{m}{\pi\hbar^2}\theta(E) \tag{1.39}$$

splits into evenly spaced peaks

$$N(E) = \frac{2eB}{h}\sum_n \delta[E - (n + \frac{1}{2})\hbar\omega_c] \tag{1.40}$$

located at each LL, and every LL has the same amount of degenerate states, $2eB/h$. The factor of 2 comes from the degeneracy of spin up and spin down electrons. Ideally, these peaks are δ functions, but in practice they spread out in energy due to disorder.

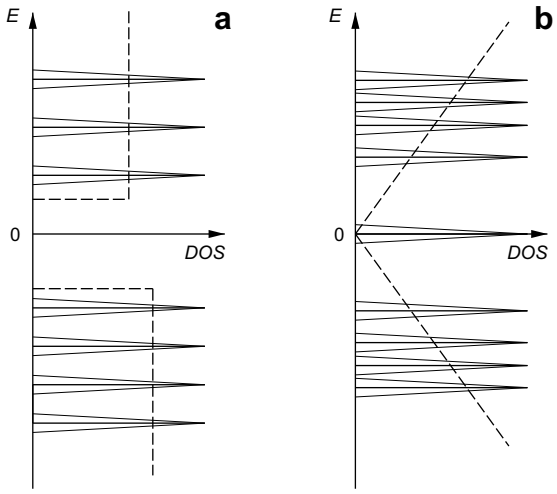

Figure 1.3: Landau level formation in (a) conventional 2D system with parabolic bands and (b) graphene with linear bands. The broken lines indicate the DOS without external magnetic field. $E > 0$ indicates electrons and $E < 0$ indicates holes. Note that there is an Landau level exactly at $E = 0$ for graphene.

This is illustrated in Fig. 1.3. Although the results above are obtained from a free electron model, the description is generally true for a electron in a crystal lattice where the energy can be approximated by a parabolic dispersion relation: $E = \hbar^2 k^2 / 2m^*$. In this case, the free electron mass m is replaced by the effective mass m^*.

We now turn to the massless Dirac fermion described by Hamiltonian 1.25. In a magnetic field, the Shrodinger equation is given by

$$-v_F(\mathbf{P} + e\mathbf{A}) \cdot \boldsymbol{\sigma}\psi(\mathbf{r}) = E\psi(\mathbf{r}) \tag{1.41}$$

where $\mathbf{P} = -i\hbar\bigtriangledown$, and $\psi(\mathbf{r})$ is a two-component vector

$$\psi(\mathbf{r}) = \begin{pmatrix} \psi_1(\mathbf{r}) \\ \psi_2(\mathbf{r}) \end{pmatrix} \tag{1.42}$$

Then we have two Equations for $\psi_1(\mathbf{r})$ and $\psi_1(\mathbf{r})$

$$-v_F(P_x - iP_y - eBy)\psi_2(\mathbf{r}) = E\psi_1(\mathbf{r}) \quad (1.43)$$

$$-v_F(P_x + iP_y - eBy)\psi_1(\mathbf{r}) = E\psi_2(\mathbf{r}) \quad (1.44)$$

Here we have again adopted Landau gauge for the vector potential $\mathbf{A}$: $\mathbf{A} = -By\widehat{x}$. Plugging Eq. 1.43 into 1.44, we obtain the equation for $\psi_2(\mathbf{r})$ only

$$v_F^2(P^2 - 2eByP_x + e^2B^2y^2 - \hbar eB)\psi_2(\mathbf{r}) = E^2\psi_2(\mathbf{r}) \quad (1.45)$$

An inspection of Eq. 1.45 reveals that it is simply Eq. 1.34, if we make the following substitution: $m \to 1/2$, $\omega_c \to 2eB$ and $E \to E^2/v_F^2$, and add a constant $-\hbar eB$ to the left hand side of Eq. 1.34. Having solved Eq. 1.34, it is trivial to find the eigenenergies of Eq. 1.45

$$E_n^2 = 2n\hbar eBv_F^2 \quad (1.46)$$

where $n = 1, 2, 3...$ The constant $-\hbar eB$ shifts the LL's by half of the equal spacing between them, and it also guarantees that there is an LL at $E = 0$, which has the same degeneracy as the other LLs. Putting them together, the eigenenergy can be written as [10, 11]

$$E_n = sgn(n)\sqrt{2e\hbar v_F^2|n|B} \quad (1.47)$$

where $n > 0$ corresponds to electron-like LLs and $n < 0$ corresponds to hole-like LLs. There is a single LL sitting exactly at $E = 0$, as a result of particle-hole symmetry.

The square root dependence of the Landau level energy on n, $E_n \propto \sqrt{n}$, can be understood if we consider the DOS for the relativistic electrons. The linear energy

spectrum of 2D massless Dirac fermions implies a linear DOS given by

$$N(E) = \frac{E}{2\pi\hbar^2 v_F^2} \tag{1.48}$$

In a magnetic field, the linear DOS collapses into LLs, each of which has the same number of states $2eB/h$. As the energy is increased, there are more states available, so less spacing between the LLs is needed in order to have the same number of state for each LL. A linear DOS directly results in a square root distribution of the LLs. This is illustrated in Fig. 1.3(b).

A wealth of information can be obtained by measuring the response of the 2D electron system in the presence of an magnetic field. One such measurement is done by passing current through the system and measure the longitudinal resistivity ρ_{xx}. As we vary the magnetic field, the energies of the LLs change. ρ_{xx} goes through one cycle of oscillation as the Fermi level moves from one LL DOS peak to the next. These are the so called Shubinikov de-Haas (SdH) oscillations. As we noticed in Eq. 1.46, the levels in a 2D massless Dirac fermion system such as graphene are shifted by one half, which means the SdH oscillations will have a phase shift of π, compared with the conventional 2D system.

The phase shift of π is a direct consequence of the Berry's phase associated with the massless Dirac fermion in graphene. To further elucidate how the chiral nature of an electron in graphene affects its motion, we resort to a semi-classical model where familiar concepts, such as the electron trajectory, provide us a more intuitive physical picture.

1.3.2 Semi-Classical Model

We consider an electron moving in a plane in a perpendicular magnetic field **B**. The basic equation of the semi-classical approach is

$$\hbar\dot{\mathbf{k}} = -e(\mathbf{v} \times \mathbf{B}) \tag{1.49}$$

which simply says that the rate of change of momentum is equal to the Lorentz force. The velocity **v** is given by

$$\mathbf{v} = \frac{1}{\hbar} \bigtriangledown_{\mathbf{k}} \epsilon \tag{1.50}$$

where ϵ is the energy of the electron. Since Lorentz force is normal to **v**, no work is done to the electron and ϵ is a constant of the motion. It immediately follows that electrons move along the orbits given by the intersections of constant energy surfaces with planes perpendicular to the magnetic fields.

Integration of Eq. 1.49 with respect to time yields

$$\mathbf{k}(t) - \mathbf{k}(0) = \frac{-eB}{\hbar} (\mathbf{R}(t) - \mathbf{R}(0)) \times \widehat{\mathbf{B}} \tag{1.51}$$

where **R** is the position of the electron in real space, and $\widehat{\mathbf{B}}$ is the unit vector along the direction of the magnetic field **B**. Since the cross product between **R** and $\widehat{\mathbf{B}}$ simply rotates **R** by 90° inside the plane of motion, Eq. 1.51 means that the electron trajectory in real space is just its k-space orbit, rotated by 90° about **B** and scaled by $\hbar/eB$.

It can be further shown that the angular frequency at which the electron moves

around the intersection of the constant energy surface is given by

$$\omega_c = \frac{2\pi eB}{\hbar^2} / \left(\frac{\partial a}{\partial \epsilon}\right)_k \tag{1.52}$$

where a is the area of the intersection (There are plenty of texts available on this topic, see e.g. [12] and [13]). For electrons having effective mass m^*, we have $\epsilon = \hbar^2 k^2/2m^*$. a is given by $\pi k^2 = 2\pi m^* \epsilon/\hbar^2$. Eq. 1.52 reduces to $\omega_c = eB/m^*$, which is the same as what we obtained previously. Comparing it with Eq. 1.52, we find

$$m^* = \frac{\hbar^2}{2\pi}\left(\frac{\partial a}{\partial \epsilon}\right)_k \tag{1.53}$$

which is actually the definition of effective mass for an arbitrary orbit.

The quantization of the electron motion will restrict the available states and give rise to the quantum oscillations such as SdH oscillations. The Bohr-Sommerfeld quantization rule for a periodic motion is

$$\oint \mathbf{p} \cdot d\mathbf{q} = (n + \gamma)2\pi\hbar \tag{1.54}$$

where $\mathbf{p}$ and $\mathbf{q}$ are canonically conjugate variables, n is an integer and integration is for a complete cycle. γ will be discussed below.

For an electron in a magnetic field,

$$\mathbf{p} = \hbar\mathbf{k} - e\mathbf{A} \qquad \mathbf{q} = \mathbf{R} \tag{1.55}$$

so Eq. 1.54 becomes

$$\oint (\hbar\mathbf{k} - e\mathbf{A}) \cdot d\mathbf{R} = (n + \gamma)2\pi\hbar \tag{1.56}$$

Plug in formula 1.51 and make use of Stokes' theorem, one finds

$$\mathbf{B} \cdot \oint \mathbf{R} \times d\mathbf{R} - \int_S \mathbf{B} \cdot d\mathbf{S} = (n + \gamma)\Phi_0 \tag{1.57}$$

where $\Phi_0 = 2\pi\hbar/e$ is the magnetic flux quanta. S is any surface in real space which has the electron orbit as the rim. Therefore the second term on the left hand side of Eq. 1.57 is just the magnetic flux $-\Phi$ penetrating the electron orbit. A closer inspection of the first term finds that it is 2Φ. Putting them together, Eq. 1.57 reduces to

$$\Phi = (n + \gamma)\Phi_0 \tag{1.58}$$

which simply means that the quantization rule dictates that the flux through the electron orbit has to be quantized.

Remember that the electron trajectory in real space is just a rotated version of its trajectory in k-space, scaled by $\hbar/eB$ (Eq. 1.51). Let $a(\epsilon)$ be the area of the electron orbit in k-space, Eq. 1.51 becomes

$$a(\epsilon_n) = (n + \gamma)2\pi eB/\hbar \tag{1.59}$$

which is the famous Onsager relation. It implicitly specifies the permitted energy levels ϵ_n (Landau Levels), which in general depends on the band structure $\epsilon(k)$.

The dimensionless parameter $0 \leq \gamma < 1$ is determined by shape of the energy band structure. For a parabolic band, $\epsilon = \hbar^2 k^2/2m^*$, the nth LL has the energy $\epsilon_n = (n + 1/2)\hbar\omega_c$. Each LL orbit in k-space is a circle with a radius $k_n = \sqrt{2eB(n + 1/2)/\hbar}$. The corresponding area of orbital in k-space for the nth LL is therefore

$$a(\epsilon_n) = \pi k_n^2 = (n + \frac{1}{2})2\pi eB/\hbar \tag{1.60}$$

A comparison of this formula with Eq. 1.59 immediately yields

$$\gamma = \frac{1}{2} \tag{1.61}$$

For massless Dirac fermion in graphene which has the linear dispersion relation $\epsilon = \hbar v_F k$, the nth LL corresponds to a circular orbit with radius $k_n = \epsilon_n/\hbar v_F = \sqrt{2e|n|B/\hbar}$. The corresponding area is therefore

$$a(\epsilon_n) = \pi k_n^2 = |n| 2\pi e B/\hbar \tag{1.62}$$

This gives

$$\gamma = 0 \tag{1.63}$$

which differs from the γ for the conventional massive fermion by $\frac{1}{2}$.

The difference of $\frac{1}{2}$ in γ is a consequence of the chiral nature of the massless Dirac fermions in graphene. An electron in graphene always has the pseudospin tied to its wave vector $\mathbf{k}$. As the electron goes through the orbit for one cycle, $\mathbf{k}$, as well as the pseudospin attached to it, goes through a rotation of 2π at the same time. Much like a physical spin, a 2π adiabatic rotation of pesudospin gives a Berry's phase of π [5]. This is exactly where the $\frac{1}{2}$ difference in γ comes from.

The above analysis can be generalized to the systems with arbitrary band structure. The work of Roth (1966) [14] and Mikitik (1999) [15] shows that the quantity γ is purely a property of the topology of the energy band structure. In general, γ can be expressed in terms of the Berry's phase, ϕ_B, for the electron orbit:

$$\gamma - \frac{1}{2} = -\frac{1}{2\pi}\phi_B \tag{1.64}$$

For any electron orbits which surround a disconnected band, as is the case for a parabolic band, this phase is zero, and we arrive at Eq. 1.61. A non-trivial Berry's phase of π results if the orbit surrounds a contact between the bands, and the energies of the bands separate linearly in $\mathbf{k}$ in the vicinity of the band contact. In graphene, these requirements are fulfilled because the valence band and conduction band are connected by $\mathbf{K}$ and $\mathbf{K}'$, and the energy dispersion is linear around these points. This again leads to a $\gamma = 0$ in graphene ($\gamma = 0$ and $\gamma = \pm 1$ are equivalent).

γ can be probed experimentally by measuring the quantum oscillation of the 2D system in the presence of a magnetic field. It is identified as the phase of such oscillations. This becomes evident when we explicitly write the oscillation part of the quantum oscillations, e.g., SdH oscillation of resistivity, $\Delta\rho_{xx}$ [8, 16, 17]

$$\Delta\rho_{xx} = R(B,T)\cos\left[2\pi\left(\frac{B_F}{B} - \gamma\right)\right] \tag{1.65}$$

Here we only take account of the first harmonic. $R(B,T)$ is the amplitude of the SdH oscillations and B_F is the frequency in $1/B$, which can be related to the 2D charge carrier density n_s by

$$B_F = \frac{n_s h}{g_s e} \tag{1.66}$$

where g_s accounts for the degeneracy of the LLs. $\gamma = 1/2$ (for parabolic band) and $\gamma = 0$ (for graphene) produces a phase difference of π between the SdH oscillation in the two types of 2D systems. In the extreme quantum limit, the SdH oscillations evolve into quantum Hall effect, a remarkable macroscopic quantum phenomenon characterized by precisely quantized Hall resistance and zeros in the longitudinal resistance. The additional Berry's phase of π manifests itself as an half-integer shift in the quantization condition, and leads to an unconventional quantum Hall effect. The experimental observation of the quantum Hall effect and Berry's phase in graphene

are reported in detail in Chapter 3 of this dissertation.

To summarize, graphene represents a new type of 2D electron system where the electrons mimic the behavior of massless, relativistic Dirac particles. The chiral nature of the electron plays a fundamental role in the transport property of graphene. First, it cause the cancelation of the backscattered electron wavefunction, and may leads to anti-localization of electron states in graphene. Second, the rotation of pseudospin in the presence of a magnetic field causes a phase shift of π in the quantum oscillation and, in extreme quantum limit, leads to an unconventional quantum Hall effect.

The organization of the this dissertation is the following:

In Chapter 2, we describe our sample preparation procedure. We present a unique micro-mechanical method ("nano-pencil" method), followed by a remarkably simple method (Scotch® tap method). We demonstrate that multi-layer as well as mono-layer graphene samples can be obtained utilizing those methods.

In Chapter 3, we report our experimental investigation of magneto-transport in high mobility ($\mu > 10^4$ cm^2/Vs) monolayer graphene samples. Adjusting the chemical potential using an electric field, we discover an unusual quantum Hall effect for both electron and hole carriers in graphene. The new type of quantum Hall effect is distinctively different from the conventional one observed in semiconductor heterotructures in that the integer quantization condition is shifted by one half. We find that the half-integer shift comes from the fact that the carriers in graphene mimic the behavior of relativistic Dirac fermions with zero mass.

The massless Dirac fermions in graphene are further probed by analyzing the SdH oscillations in graphene. Our data show a phase shift of π in the SdH oscillations, which corresponds to a Berry's phase of π associated with the energy band of graphene. This result supports the existence of such massless Dirac fermion in

graphene. The effect mass of the carriers in graphene, m^*, is measured at different energies, E_F. The result fits very well with Einstein's equation, $E_F = m^* v_F^2$, where the speed of light is replaced with the constant Fermi velocity in graphene v_F, providing further evidence that the carriers in graphene is indeed effectively relativistic.

In Chapter 4, we report the quantum Hall (QH) effect observed in our graphene samples in strong magnetic fields up to 45 T. QH states at filling factors $\nu = 0, \pm 1, \pm 4$ are discovered at fields $B > 20$ T, indicating the lifting of the four-fold degeneracy of the previously observed QH states at $\nu = \pm 4(|n| + 1/2)$, where n is the Landau level index. In particular, the presence of the $\nu = 0, \pm 1$ QH states indicates that the Landau level at the charge neutral Dirac point splits into four sub-levels, lifting both sublattice and spin degeneracy. We also investigate the QH effect at $\nu = \pm 4$ in tilted magnetic fields and conclude that $\nu = \pm 4$ QH states can be attributed to lifting of the $n = \pm 1$ spin-degeneracy of the Landau level.

In Chapter 5, we study multi-layer graphene with thicknesses ranging from 12 – 90 nm. Strong conductance modulation as a function of gate voltage is reported in the thinner crystallite devices, owning to the mesoscopic nature of these samples. The temperature-dependent resistivity data from devices of varying thicknesses are explained in the framework of a simple two-band model. The reduced mobility in thinner samples indicates increased boundary scattering contribution in the thinner graphite samples. The galvanomagnetic transport properties of these mesoscopic devices are studied in the presence of an external magnetic field. We observe strong modulation of magneto-resistance and Hall resistance as a function of the gate voltage as the sample thickness approaches the screening length of graphite. Such strong modulation allows us to detect the electric field dependent Landau level formation from Shubnikov-de Haas oscillations. The effective mass of electron and hole carriers

has been measured from the temperature dependent behavior of these oscillations, and they agree with the values from the measurement of the bulk graphite very well.

In Chapter 6, we recapitulate the major conclusions of this dissertation.

Chapter 2

Sample Preparation

2.1 Overview

Generally speaking, various methods that are developed in trying to get single sheets of graphene fall into two categories: the bottom-up approach and the top-down approach. Following the bottom-up approach, one starts with carbon atoms and tries to assemble graphene sheets from those atoms by chemical pathways [18, 19]. This is best exemplified by work of W. A. de Heer group in Georgia Institute of Technology. In Ref. [19], they demonstrated that thin graphite films can be grown by thermal decomposition on the (0001) surface of 6H-SiC. This method opens the way to large scale integration of nanoelectronics based on graphene, but so far the growth and identification of monolayer graphene remains an obstacle.

On the other hand, the top-down approach starts with bulk graphite, which is essentially graphene sheets stacked together, and tries to extract graphene sheets from the bulk by mechanically. The mechanical extraction of layered material dates back to the 70s. In his seminal experiment [20], Frindt showed that few layers of

superconductor $NbSe_2$ can be mechanically cleaved from the bulk crystal fixed on an insulating surface by epoxy. While it is known for decades that people routinely cleave graphite using scotch tape when preparing sample surface for Scanning Tunneling Microscopy (STM) study, the first pointed experiment involving mechanical cleaving of graphite using scotch tape was carried out by Ohashi et al. [21]. The thinnest graphite film obtained in this experiment was 10 nm, corresponding to $\sim$ 30 layers. It is worth noting that patterning of bulk graphite prior to the mechanical cleaving can be done with oxygen plasma etching [22]. A patterned graphite surface offers a better control over the cleaving process.

The past two years saw booming activities on mechanical cleaving of graphite. Various methods were implemented. However, not until 2004 were few-layer graphene sheets extracted from bulk graphite, using a remarkably simple method ("Scotch tape method"), which will be discussed in detail in 2.3.

In this chapter, I will first describe our unique micro-mechanical method ("Nano-pencil"), with which graphite crystallites with thicknesses down to 12 nm are obtained. The "Scotch tape method" will be discussed in section 2.3.

2.2 Nano-Pencil

While simple mechanical cleaving proved to be a reliable way to get thin graphite crystallites down to $\sim$ 10 nm [21, 22], one may speculate that a more controlled cleaving yield thinner, potentially monolayer, crystals. We develop a micro-mechanical cleaving process which exploits the precise force and position controllability of the Atomic Force Microscope (AFM). The key for such a process is the AFM cantilever with micron-sized graphite block mounted as the tip. Much like writing with a pencil, by

operating the AFM in contact mode, the graphite tip scratches the substrate with precisely controlled force and speed.

The graphite tip is made from bulk Highly Oriented Pyrolytic Graphite (HOPG). Using a similar technique demonstrated in [22], arrays of graphite micro-pillars ($\sim 2 \times 2 \times 5$ μm^3) are fabricated on the HOPG surface using micro-patterning followed by masked anisotropic oxygen plasma etching (Plasma-Therm PK-12 RIE). During the etching process, oxygen flow rate is maintained at 20 sccm and pressure 50 mTorr. Once the array is formed (Fig. 2.1(a) inset), an individual block of the pillar is removed from the surface using a precision micro-manipulator (Newport, 461 Series) above an inverted optical microscope with 500$\times$ resolution. The detached graphite block is then transferred to a micro-machined silicon cantilever (MikroMasch), where it is glued down by a small amount of ultra-violet sensitive epoxy (Millennium EN239-2), as shown in Fig. 2.1(a).

In the next step, we use the mounted graphite block on the cantilever as the tip of an atomic force microscope (AFM) in order to transfer thin graphite samples onto a SiO_2/Si substrate for subsequent device fabrication. By operating the AFM (Nanoscope IIIa Multimode, Digital Instruments) in contact mode with load on the graphite mounted cantilever, very thin layers of HOPG are sheared off onto the substrate (Fig.2.1(b)). This microscopic cleaving process can be controlled by tuning the normal force between the cantilever and the substrate. The van der Waals binding energy between the graphene layers in graphite is $\sim$ 2 eV nm^{-2} [23]. Assuming the graphite-substrate friction coefficient is $\sim$ 1, the required normal force to cleave off a 1 μm^2 graphite sheet from the top of the crystallite is $\sim$ 300 nN. A normal force in the range of 10 - 2000 nN can be easily managed by commercially available silicon cantilevers. In our experiment, by fine tuning the normal force and the scanning

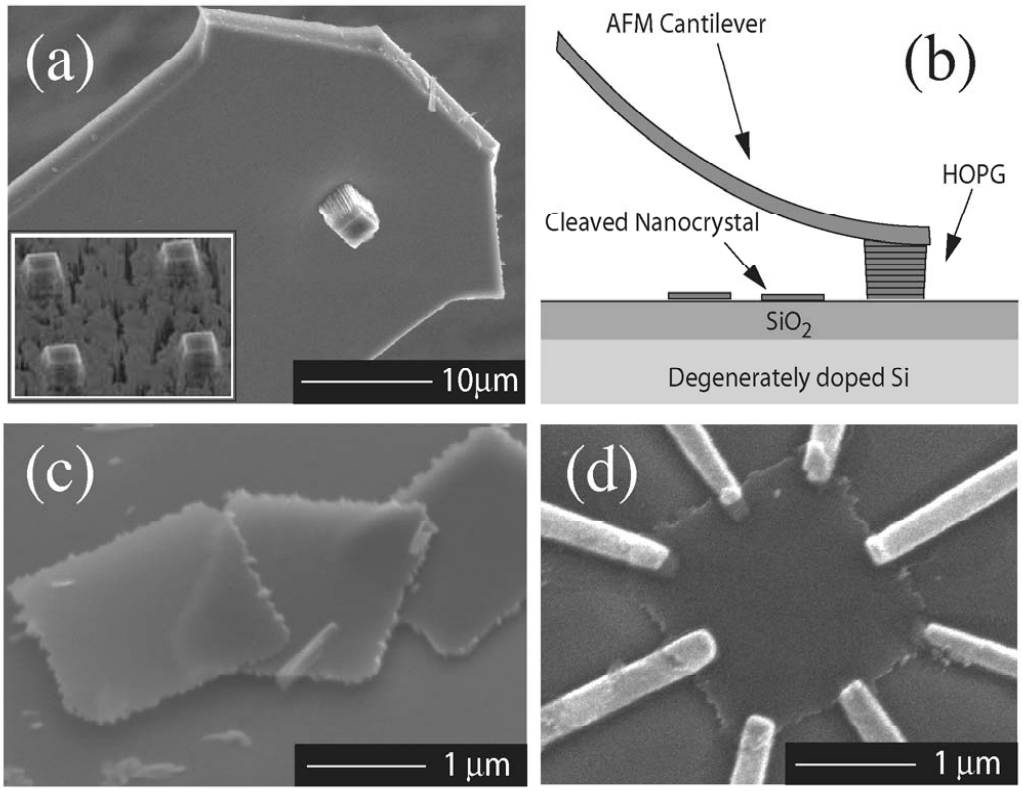

Figure 2.1: Micro-mechanical cleaving of HOPG using "nano-pencil". (a) scanning electron microscope image of an HOPG crystallite mounted on a microcantilever. Inset: Bulk HOPG surface patterned by masked anisotropic oxygen plasma etching. (b) Schematic drawing of the micro-cleaving process. (c) Thin graphite samples cleaved onto the SiO_2/Si substrate. (d) A typical mesoscopic device fabricated from a cleaved graphite sample.

speed of the cantilever (1-10 μm/sec), square graphite crystallites with lateral size $\sim$ 2 μm and thicknesses ranging from 10 - 100 nm are easily obtained (Fig.2.1(c)). Once the graphite samples are cleaved onto a substrate with predefined alignment marks, AFM images are acquired for measuring the height of the cleaved crystallites and registering the position for device design. The measured surface roughness of the samples are less than 0.5 nm, and we do not observe any appreciable number of step edges with height larger than 0.5 nm.

In figure 2.1(d) we show a thin graphite device for electronic transport measurements. The electrodes are fabricated using electron beam lithography, followed by metal thermal evaporation (Cr/Au=3/60nm) and overnight lift-off in acetone.

2.3 The Legend of Scotch Tape

The micro-mechanical cleaving described above is a delicate and sometimes time consuming process. Although it provides a reliable way of obtaining graphite crystals with thickness $\sim$ 10 nm, its low throughput makes it difficult to get to monolayer graphene. Most of the pieces that are cleaved onto the SiO_2/Si substrate are multiple layer crystals, therefore a large statistics is needed in order to find a potential monolayer crystal. Hence comes the idea of massive, direct cleaving using bulk graphite.

The procedure is remarkably simple, as first reported by Novoselov et al.[7]. We start with graphite flakes(Kish, Toshiba Ceramics), and rub them against a flat SiO_2/Si substrate directly, using a piece of adhesive tape (Stoch® tape) as a holder. During cleaving, the graphite flakes make intimate contact with the substrate at many different locations. At each of those locations, there is one "nano-pencil" at work. Although the probability of obtaining monolayer graphene for each such "nano-pencil"

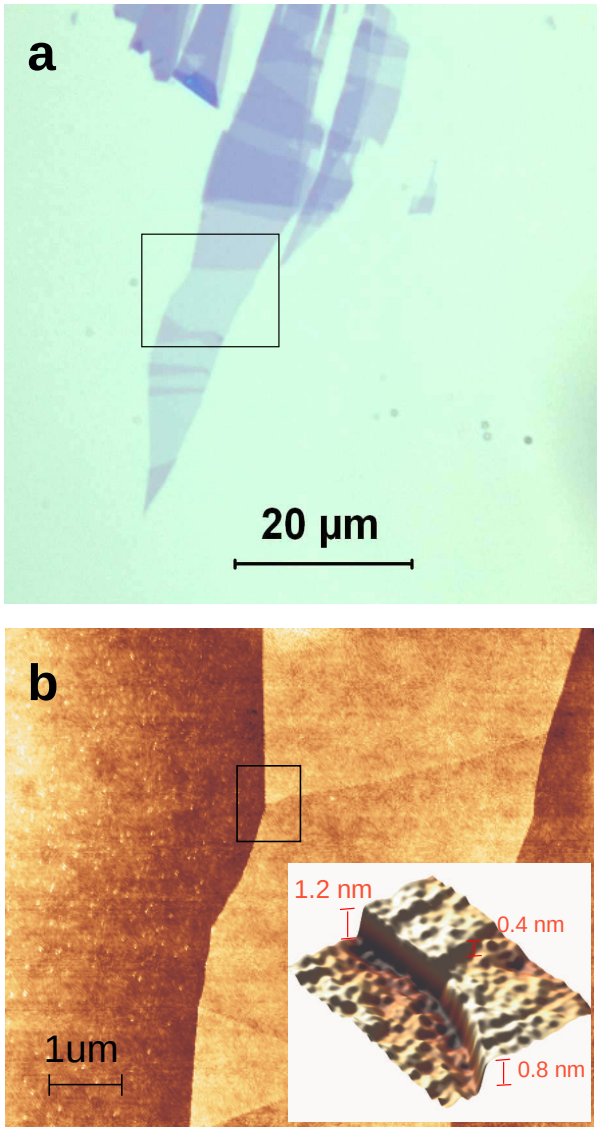

Figure 2.2: Cross-correlation of optical microscope and AFM images of few-layer graphene samples. (a) An optical microscope image of micro-cleaved graphite samples deposited on a SiO_2/Si substrate. (b) An AFM image of potentially single and double layer graphene samples discovered in the boxed region of (a). The inset shows a detailed AFM height profile in the boxed region of the main panel.

is small, with thousands of them working in parallel, we can always find single layers, among the great majority of other thicker flakes that are cleaved onto the substrate. In short, by sacrificing controllability, we gain on statistics.

After cleaving, the key for finding single layers amid thicker flakes is visual identification using an optical microscope. Graphene monolayers are clearly visible on a Si wafer with thermally grown SiO_2 layer (Fig. 2.2a), due to the interference induced color shift. The thickness of SiO_2 layer significantly affects the visibility of single layers and the contrast between layers with different thicknesses. We find that ~ 290 nm thick thermally grown SiO_2 layer yields the best contrast for this purpose.

In order to measure thickness of deposited graphene layers, a cross-correlation study between optical microscope and AFM images was made. As shown in Fig. 2.2a, there are color contrast changes in the samples with different thicknesses due to interference induced color shifts. These color shifts are sensitive to the number of graphene layers on the top of the SiO_2/Si substrate. Once the optical images are taken, the sample profiles are probed using AFMs (MultiMode AFM, Digital instrument and XE100, PSIA). For example, Fig. 2.2b shows an AFM image of samples in the boxed region in 2.2a. The detailed AFM height profile analysis (inset) yields the apparent height of region (I) and (II) are 0.8 nm and 1.2 nm, respectively. An atomic layer step (0.4 nm high) is observed between the region (I) and (II), indicating the region (II) has just one more layer of graphene. Since a single sheet of graphene is 0.35 nm thick, the region (I) is comprise of at the most two graphene layers. However, considering an additional van der Waals (vdW) distance between graphene and SiO_2 surface (0.3 nm) [24], we speculate that the region (I) is most likely a single layer, unless the AFM tip to graphene interaction is much stronger than that of the AFM tip to SiO_2 interaction. This is highly unlikely, since AFM profile analysis

has been faithfully used for determining diameter of carbon nanotubes, a material that share a similarity with graphene, where well established cross-correlation between AFM determined diameter and Raman spectroscopy determined diameter [25].

In addition, the electronic transport signal from the sample can be used to distinguish the monolayer from bilayer graphene as they exhibit distinctively different quantum Hall effects. This will be discussed in Chapter 3.

Chapter 3

Monolayer Graphene

3.1 Sample Characterization

The monolayer graphene samples used in this study are obtained using the Stoch® tape method described in Chapter 2. After single layers of graphene are cleaved onto SiO_2/Si substrate, their position is determined with respect to pre-defined align marks. A subsequent electron beam lithography process locates the graphene samples and defines thermally evaporated electrodes (Cr/Au = 3/60 nm) on top, followed by overnight liftoff in acetone. We have used typical electron beam lithography conditions. Single layer of 950 molecular weight Polymethyl Methacrylate (PMMA) is spin-coated at 4000 RPM onto the sample, then baked at 180°C for 2 minutes prior to exposure to 30 keV electron beam. The electron beam dosage is set at 450 μC/cm^2. The electrodes are typically arranged into a Hall-bar geometry (see the inset of Fig. 3.1a for picture of a typical device). The devices are fabricated on degenerately doped Si wafers with $\sim$ 300 nm thermally grown SiO_2. The Si underneath serves as a back gate, which is used to tuned the charge density in the graphene samples.

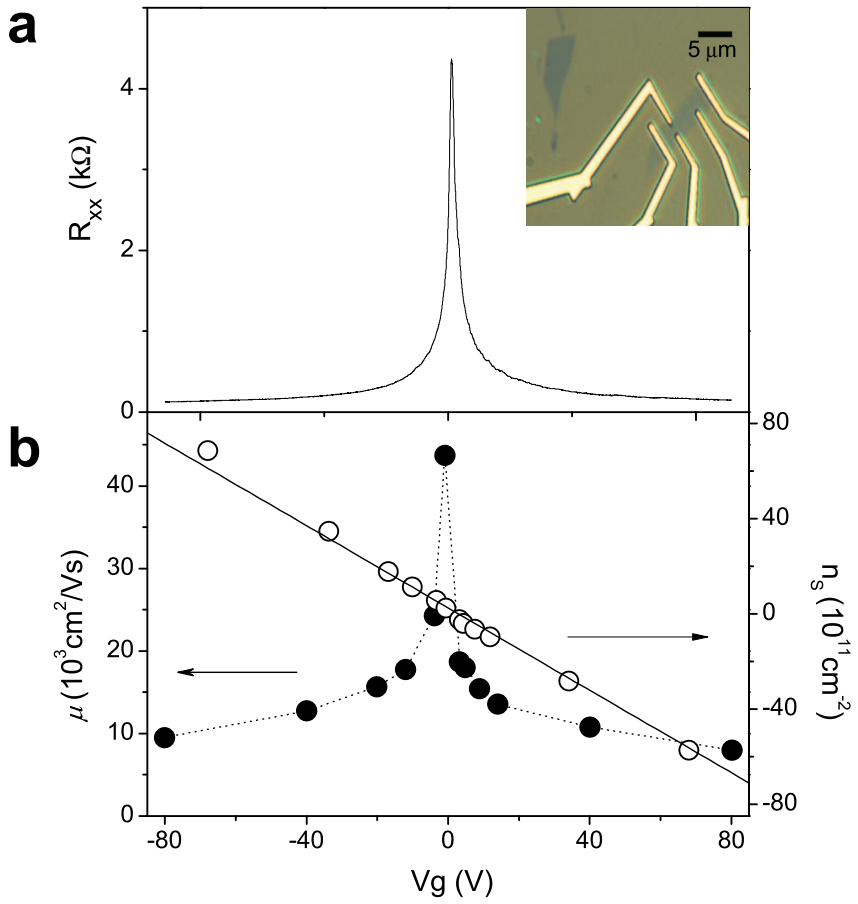

Figure 3.1: Resistance, carrier density, and mobility of graphene measured at 1.7 K at different gate voltages. (a) Resistance changes as a function of gate voltage in a graphene device shown in the optical microscope image in the right inset. The position of the resistance peaks varies from device to device, but the peak values are always of the order of ~ 4 kΩ, suggesting a potential quantum mechanical origin. The left inset shows a schematic diagram for the low energy dispersion relation near the Dirac points in the graphene Brillouin zone. Only two Dirac cones are inequivalent to each other, producing a two-fold valley degeneracy in the band structure. (b) Charge carrier density (open circle) and mobility (filled circle) of graphene as a function of gate voltage. The solid line corresponds to the estimated charge induced by the gate voltage, $n_s = C_g V_g/e$, assuming a gate capacitance $C_g = 115$ μF/m^2 obtained from geometrical consideration.

Most of our electronic transport measurements are performed in a variable temperature cryostat (Janis VariTemp) with temperatures ranging from 1.6 – 300 K, where samples are cooled by continuous flowing helium vapor. The temperature control is achieved by applying heating power to the heater on the sample probe, using a Lakeshore 340 temperature controller. An external magnetic field perpendicular to the graphene plane can be applied using a superconducting magnet. The magnet is controlled by Model CS4 bipolar power supply from Cryomagnetics, Inc. For extremely low temperature measurements, we use a dilution refrigerator where temperatures as low as 30 mK can be reached. The magneto-resistance (R_{xx}) and Hall resistance (R_{xy}) of the graphene samples are measured using Lock-in amplifiers with an excitation current of 10 nA at a frequency $\sim$ 13 Hz.

Fig.3.1a shows the gate modulation of R_{xx} at zero magnetic field in a typical graphene device whose lateral size is $\sim$ 3 μm. While R_{xx} remains in the $\sim$ 100 Ω range at high carrier density, a sharp peak whose value is on the order of $\sim$ 4 kΩ is observed at $V_g \approx 0$ V. While different samples show slightly different peak values and peak positions, similar behaviors were observed in at least 10 other graphene samples we have measured. The existence of such a sharp peak is consistent with the reduced carrier density as E_F approaches the Dirac point of graphene where the density of states vanishes. Thus the gate voltage corresponding to the charge neutral Dirac point, V_{Dirac}, can be determined from this peak position.

A separate measurement of R_{xy} provides a measure for the sheet carrier density, n_s, of the sample. Assuming a simple Drude model, n_s can be obtained from the linear dependence of the Hall resistance R_{xy} on the magnetic field, B, in the low field limit, $B \to 0$

$$n_s = \left[e \frac{\mathrm{d}R_{xy}}{\mathrm{d}B} \right]^{-1} \tag{3.1}$$

Combined with R_{xx} measurement, the carrier mobility, μ, can be calculated using the following formula

$$\mu = \frac{1}{en_s\rho_{xx}} \tag{3.2}$$

where

$$\rho_{xx} = R_{xx}\frac{W}{L} \tag{3.3}$$

with W and L the width and length of the sample respectively.

The sheet carrier density and mobility at different gate voltages are plotted in Fig. 3.1. The sign of n_s changes at $V_g = V_{Dirac}$, indicating E_F indeed crosses the charge neutral point. Mobilities are higher than 10^4 cm^2/Vs for the entire gate voltage range, considerably exceeding the quality of previously studied graphene samples[19, 24].

3.2 Unconventional Integer Quantum Hall Effect

The exceptionally high mobility graphene samples allow us to investigate transport phenomena in the extreme magnetic quantum limit, such as the quantum Hall Effect (QHE) [8].

QHE was discovered by von Klitzing et al. in the 2D electron gas in the inversion layer of a MOSFET (metal-oxide-semiconductor field-effect-transistor) in 1980 [26]. Since then, it has become one of the most active field of research in condensed matter physics. QHE occurs in 2D electron system at low temperatures and strong perpendicular magnetic field. It is characterized by plateaus of the Hall conductivity quantized at integer multiples of the universal constant e^2/h

$$R_{xy}^{-1} = g_s n e^2/h \tag{3.4}$$

accompanied by a vanishing longitudinal resistivity, a signature of a dissipationless current flow. Here g_s is the degeneracy of the LLs, and n is a positive integer. Graphene, on the other hand, represents a new type of 2D electron system where the carriers can be treated as massless Dirac fermions. The QHE in such a system will provide important information about quantum electrodynamics in 2D.

Fig. 3.2a shows R_{xy} and R_{xx} of the sample of Fig. 3.1 as a function of magnetic field B at a fixed gate voltage $V_g > V_{Dirac}$. The overall positive R_{xy} indicates that the contribution is mainly from electrons. At high magnetic field, $R_{xy}(B)$ exhibits plateaus and R_{xx} is vanishing, which are the hallmark of the QHE. At least two well-defined plateaus with values $(2e^2/h)^{-1}$ and $(6e^2/h)^{-1}$, followed by a developing $(10e^2/h)^{-1}$ plateau, are observed before the QHE features transform into Shubnikov de Haas (SdH) oscillations at lower magnetic field. The quantization of R_{xy} for these first two plateaus is better than 1 part in 10^4, precise within the instrumental uncertainty. We observe the equivalent QHE features for holes ($V_g < V_{Dirac}$) with negative R_{xy} values (Fig. 3.2a, inset). Alternatively, we can probe the QHE in both electrons and holes by fixing the magnetic field and changing V_g across the Dirac point. In this case, as V_g increases, first holes ($V_g < V_{Dirac}$) and later electrons ($V_g > V_{Dirac}$) are filling successive Landau levels and exhibit the QHE. This yields an antisymmetric (symmetric) pattern of R_{xy} (R_{xx}) in Fig. 3.2b, with R_{xy} quantization accordance to

$$R_{xy}^{-1} = \pm g_s(n + \frac{1}{2})e^2/h \tag{3.5}$$

where n is a non-negative integer, +/- stands for electrons and holes respectively. This quantization condition can be translated to the quantized filling factor, ν, in the usual QHE language. Here in the case of graphene, $g_s = 4$, accounting for 2 spin degeneracy and 2 sub-lattice degeneracy, i.e **K** and **K′** degeneracy. In addition,

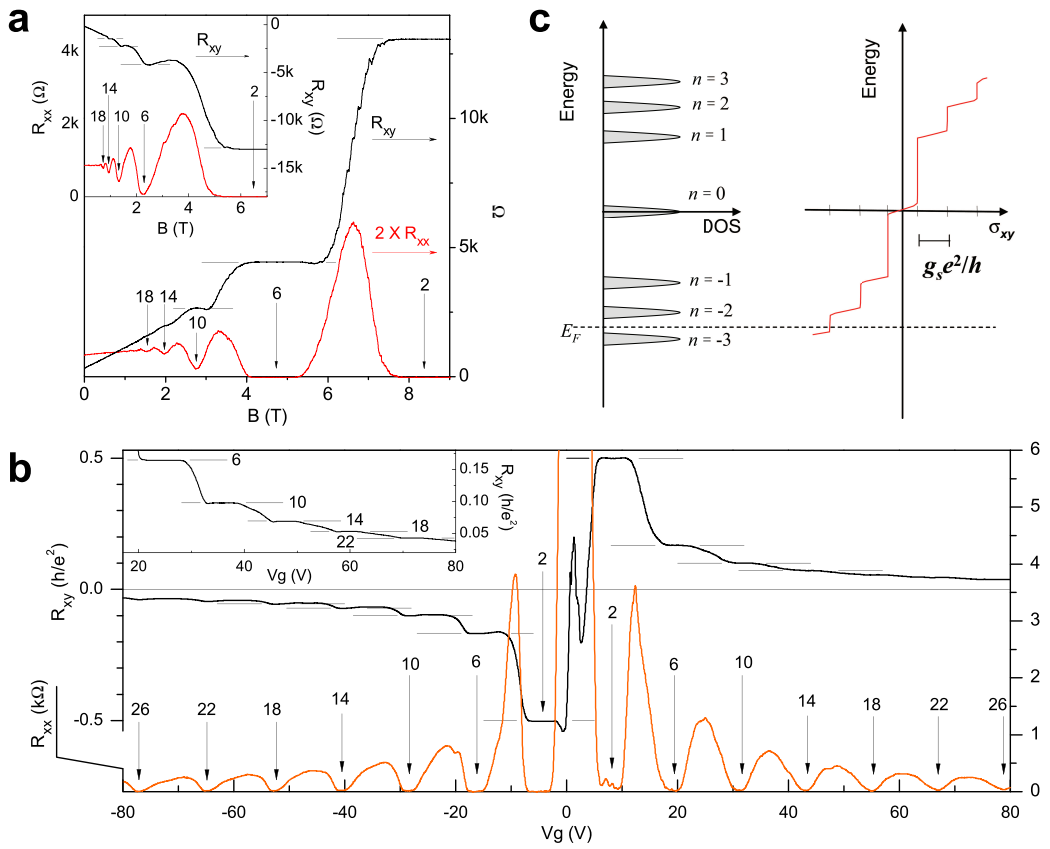

Figure 3.2: Quantized magnetoresistance and Hall resistance of a graphene device. (a) Hall resistance (black) and magnetoresistance (red) measured in the device in Fig. 3.1 at $T = 30$ mK and $V_g = 15$ V. The vertical arrows and the numbers on them indicate the values of B and the corresponding filling factor ν of the quantum Hall states. The horizontal lines correspond to $h/\nu e^2$ values. The QHE in the electron gas is demonstrated by at least two quantized plateaus in R_{xy} with vanishing R_{xx} in the corresponding magnetic field regime. The inset shows the QHE for a hole gas at $V_g = -4$ V, measured at 1.6 K. The quantized plateau for filling factor $\nu = 2$ is well-defined and the second and the third plateau with $\nu = 6$ and 10 are also resolved. (b) The Hall resistance (black) and magnetoresistance (orange) as a function of gate voltage at fixed magnetic field $B = 9$ T, measured at 1.6 K. The same convention as in a is used here. The upper inset shows a detailed view of high filling factor plateaus measured at 30 mK. (c) A schematic diagram of the Landau level density of states (DOS) and corresponding quantum Hall conductance (σ_{xy}) as a function of energy. Note that in the quantum Hall states, $\sigma_{xy} = -R_{xy}^{-1}$. The LL index n is shown next to the DOS peak. In our experiment, the Fermi energy E_F can be adjusted by the gate voltage, and R_{xy}^{-1} changes by an amount of $g_s e^2/h$ as E_F crosses a LL.

there is an oscillatory structure developed near the Dirac point. This structure is reproducible, and it is later (Chapter 4) revealed that this is due to a developing $\nu = 0$ at the Dirac point.

The observed QHE in graphene is distinctively different from those 'conventional' QHEs because of the additional half-integer in the quantization condition (Eq. 3.5). This unusual quantization condition is a result of the topologically exceptional electronic structure of graphene, which we shall discuss in the next section. The sequence of half-integer multiples of quantum Hall plateaus has been predicted by several theories which combine 'relativistic' Landau levels with the particle-hole symmetry of graphene [27–29]. This can be easily understood from the calculated LL spectrum (Eq. 1.47) as shown in Fig. 3.5c. Here we plot the density of states (DOS) of the g_s-fold degenerate (spin and sublattice) LLs and the corresponding Hall conductance ($\sigma_{xy} = -R_{xy}^{-1}$, for $R_{xx} \to 0$) in the quantum Hall regime as a function of energy. σ_{xy} exhibits QHE plateaus when E_F (tuned by V_g) falls between LLs, and jumps by an amount of $g_s e^2/h$ when E_F crosses a LL. Time reversal invariance guarantees particle-hole symmetry and thus σ_{xy} is an odd function in energy across the Dirac point[11]. However, in graphene, the $n = 0$ LL is robust, i.e., $E_0 = 0$ regardless of the magnetic field, provided that the sublattice symmetry is preserved[11]. Thus the first plateau of R_{xy}^{-1} for electron ($n = 1$) and hole ($n = -1$) are situated exactly at $g_s e^2/2h$. As E_F crosses the next electron (hole) LL, R_{xy}^{-1} increases (decreases) by an amount of $g_s e^2/h$, which yields the quantization condition in Eq. 3.5.

We also note that graphene bilayer exhibits a different QHE, as shown in Fig. 3.3. In contrast to monolayer graphene, the Hall resistance graphene bilayer is quantized according to $R_{xy}^{-1} = g_s n e^2/h$, accompanied by vanishing R_{xx}. This distinctive quantization condition can be used to differentiate graphene monolayer and bilayer. A

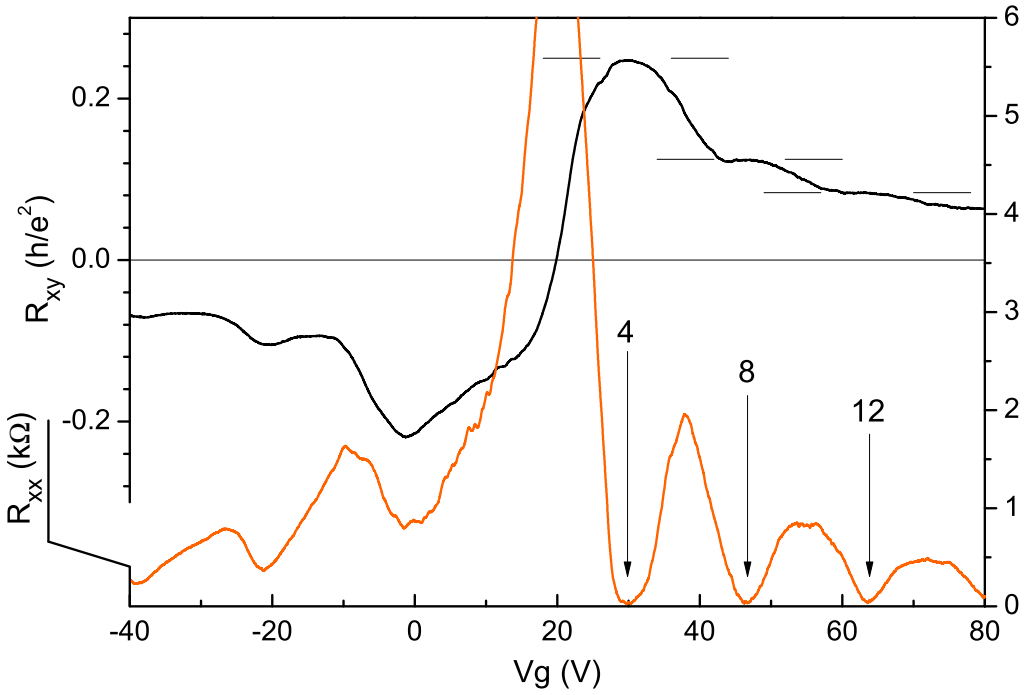

Figure 3.3: Magnetoresistance and Hall resistance of a bilayer graphene sample as a function of gate voltage. Hall resistance (black) and magnetoresistance (orange) are measured at $T = 1.7$ K and $B = 14$ T. While hole carrier side ($V_g < 20$ V) does not show the QHE, the electron carriers ($V_g > 20$ V) do exhibit the QHE, with the filling factor is expressed by integer $\nu = g_s n$, where n = 1, 2, 3 ..., unlike the half-integer QHE observed in single layer graphene. The vertical arrows and numbers on them indicate the values of B and the corresponding filling factor. The horizontal lines correspond to $h/\nu e^2$.

close investigation [30, 31] shows that a graphene bilayer itself represents another new 2D system in which coupling between two graphene monolayer transform the massless Dirac fermions into massive chiral fermions. Unlike Dirac fermions, the chiral fermions in graphene bilayer have a Berry's phase of 2π upon a 2π rotation in $\mathbf{k}$ space. This corresponds to a eight-fold degenerate LL at zero energy, and all other LLs have a degeneracy of 4.

3.3 Measurement of Berry's Phase

As discussed in Chapter 1, a consequence of the combination of time reversal symmetry with the novel Dirac point structure can be viewed in terms of Berry's phase arising from the band degeneracy point[15, 32]. A direct implication of Berry's phase in graphene is discussed in the context of the quantum phase of a spin-1/2 pseudospinor that describes the sublattice symmetry [5, 16]. This phase is already implicit in the half-integer shifted quantization rules of the QHE. It can further be probed in the magnetic field regime where a semi-classical magneto-oscillation description holds [17, 33]. Reproducing Eq. 1.65, the first harmonic of SdH can be written as

$$\Delta\rho_{xx} = R(B,T)\cos\left[2\pi\left(\frac{B_F}{B} + \frac{1}{2} + \beta\right)\right] \tag{3.6}$$

Here $R(B,T)$ is the SdH oscillation amplitude, B_F is the frequency of the SdH oscillation in $1/B$, and $\beta = \frac{1}{2} - \gamma$ is the associated Berry's phase (divided by 2π) of value $-1/2 < \beta \leq 1/2$. Berry's phase $\beta = 0$ corresponds to the trivial case. A deviation from this value is indicative of interesting new physics with $\beta = 1/2$ (or equivalently $\beta = -1/2$ implying the existence of Dirac particles [15].

Experimentally, this phase shift in the semi-classical regime can be obtained from

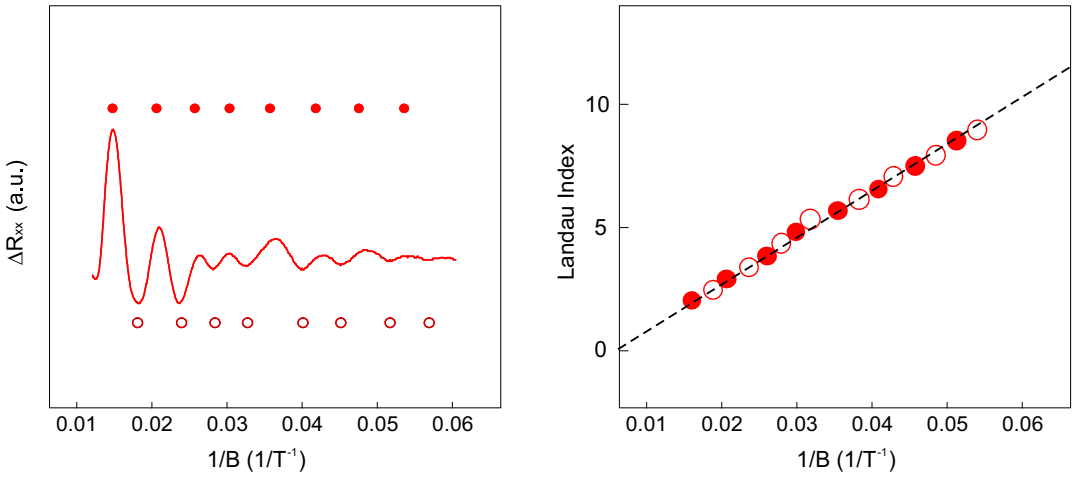

Figure 3.4: An example of the SdH fan diagram. (a) The oscillatory part of the longitudinal resistance, ΔR_{xx}, plotted as a function of $1/B$. The peaks and valleys are indicated by solid and open circles, respectively. (b) The Landau index of each oscillation plotted against its location in terms of $1/B$ in (a). The slope of the linear fit (broken line) yields the oscillation frequency, B_F, and the y-axis intercept yields the Berry's phase, β, in the unit of π.

an analysis of the SdH fan diagram. An example of the SdH fan diagram is given in Fig. 3.4. We first locate the peaks and valleys of the SdH oscillations in terms of $1/B$, then plot them against their Landau index n. The slope of a linear fit to the data points gives the SdH oscillation frequency, B_F, which is related to the sheet carrier density (Eq. 1.66). The intercept of the linear fit with the n-index axis yields Berry's phase, β, in the unit of π, modulo an integer.

Fig. 3.5 shows SdH fan diagram for graphene at different gate voltages. Remarkably, the resulting β is very close to 0.5 (upper inset to Fig. 3.5) for all the gate voltages, providing further manifestation for the existence of a non-zero Berry's phase in graphene and the presence of Dirac particles. Such a non-zero Berry's phase was not observed in the previous few layer graphite specimens [24, 33, 34], although there have been claims of hints of a phase shift in earlier measurements on bulk graphite[17].

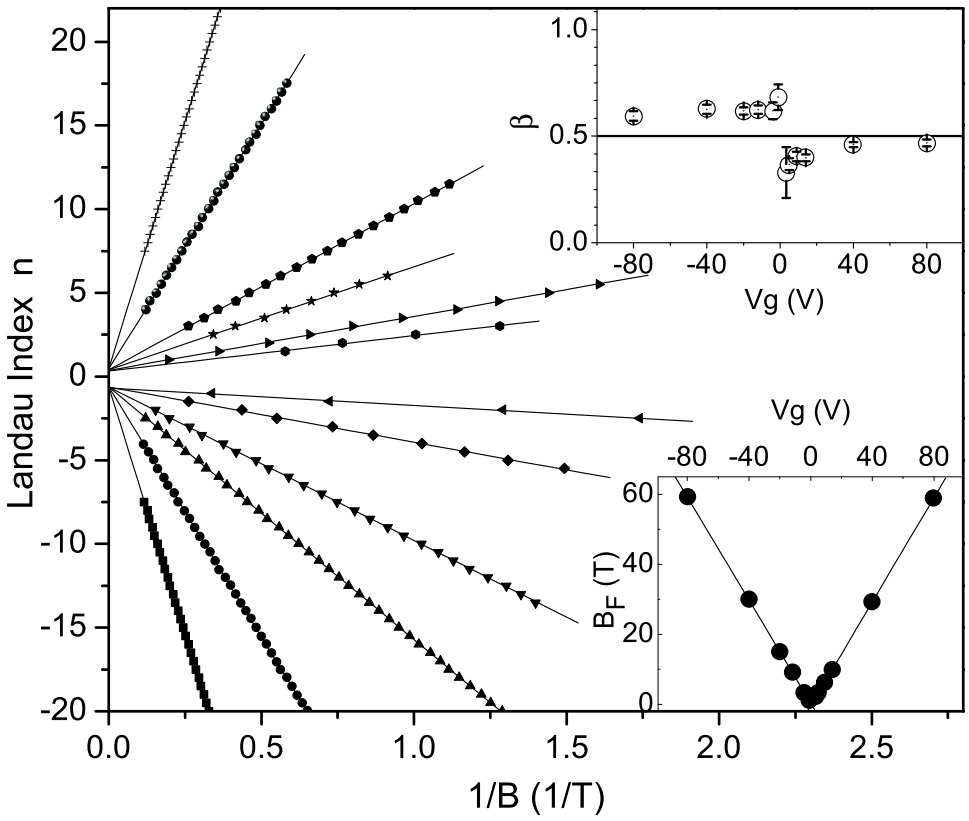

Figure 3.5: Measurement of Berry's Phase in Graphene. Landau fan diagrams are shown for SdH oscillations at different gate voltages. The location of $1/B$ for the nth minimum of R_{xx} counting from $B = B_F$ is plotted against n. The lines correspond to a linear fit, where the slope (lower inset) indicates B_F and the n-axis intercept (upper inset) provides a direct probe of Berry's phase in the magneto-oscillation in graphene.

Our data for graphene provide indisputable evidence for such an effect in a solid state system.

3.4 “Relativistic” Effective Carrier Mass

The non-zero Berry’s phase observed in the SdH fan diagram is related to the vanishing mass at the Dirac point. We can extract this effective carrier mass mc from the temperature dependence of the well developed SdH oscillations at low B-field (Fig. 3.6 left inset) using the standard SdH formalism[13]. Indeed, the analysis at different gate voltages yields a strong suppression of m_c near the Dirac point. While the high density ($n_s \sim 5 \times 10^{12}$ cm^{-2}) carrier gas shows $m_c \approx 0.04 m_e$, the mass drops to $m_c \approx 0.007 m_e$ near the Dirac point ($n_s \sim 2 \times 10^{11}$ cm^{-2}), where m_e is the free electron mass. Overall, the observed gate voltage-dependent effective mass can be fit to the ‘relativistic’ mass:

$$m_c = \frac{E}{v_F^2} = \sqrt{\pi \hbar^2 n_s / v_F^2} \tag{3.7}$$

using v_F as the only fitting parameter (Fig. 3.6 right inset). In accordance with the Berry’s phase argument, this procedure extrapolates to a vanishing mass at the Dirac point.

3.5 Conclusion

In conclusion, we have experimentally discovered an unusual QHE in high quality graphene samples. Unlike conventional 2D systems, the observed quantization condition in graphene is described by half-integer rather than integer values. The half-integer quantization condition, as well as the measured phase shift in magneto-

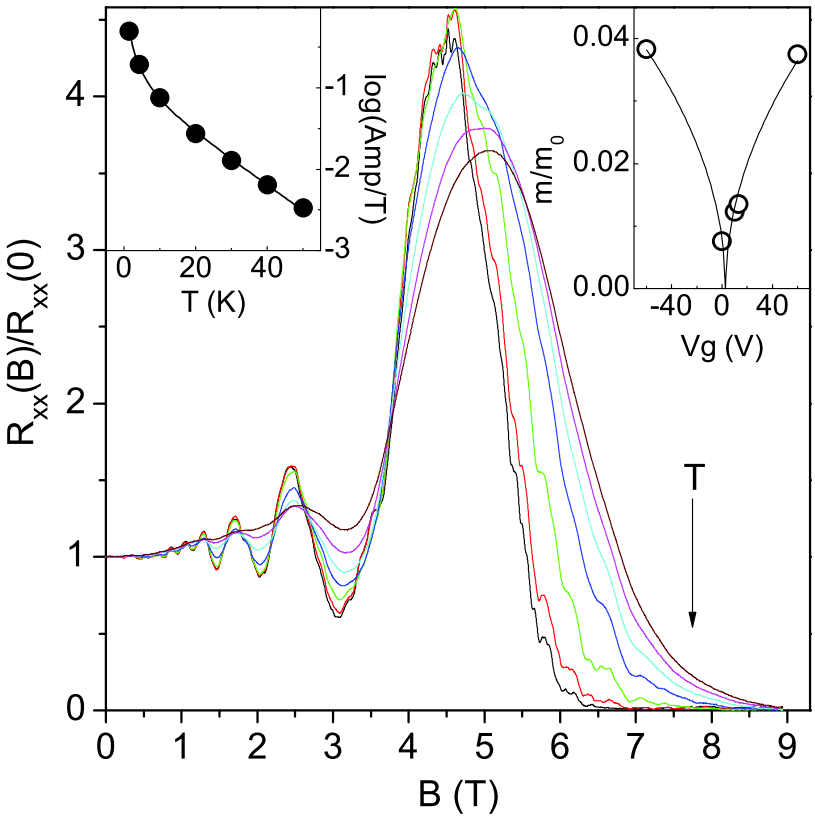

Figure 3.6: Effective mass measurement from the temperature dependence dependence of the Shubnikov de Haas oscillations in graphene. Main panel: Temperature dependence of the SdH oscillations at $V_g = -2.5$ V. Each curve represents $R_{xx}(B)$ normalized to $R_{xx}(0)$ at a fixed temperature. The curves are in order of decreasing temperature starting from the top as indicated by the vertical arrow. The corresponding temperatures are listed in the left inset. The left inset represents the SdH oscillation amplitude divided by temperature measured at a fixed magnetic field. The standard SdH fit yields the effective mass. The right inset is a plot of the effective mass obtained at different gate voltages. The solid line is a fit to the single parameter model described in the text, which yields $v_F = 1.1 \times 10^6$ m/s, in reasonable agreement with the literature values.

oscillation, can be attributed to the peculiar topology of the graphene band structure, specifically the linear dispersion relation and the implied vanishing mass near the Dirac point. The electron dynamics due to this band structure can be described in terms of "relativistic" carriers. The unique behavior of electrons in this newly discovered $(2 + 1)$-dimensional quantum electrodynamics system not only opens up many interesting questions in mesoscopic transport in electronic systems with non-zero Berry's phase but may also provides the basis for novel carbon based electric and magnetic field effect device applications, such as ballistic metallic/semiconducting graphene ribbon devices and electric field effective spin transport devices utilizing spin-polarized edge state[35].

Chapter 4

Magneto-transport in Graphene in High Magnetic Field

In this Chapter, we report the quantum Hall (QH) effect in two-dimensional (2D) electrons and holes in high quality graphene samples in strong magnetic fields up to 45 T [36]. QH states at filling factors $\nu = 0, \pm 1, \pm 4$ are discovered at fields $B > 20$ T, indicating the lifting of the four-fold degeneracy of the previously observed QH states at $\nu = \pm 4(|n| + 1/2)$, where n is the Landau level index. In particular, the presence of the $\nu = 0, \pm 1$ QH states indicates that the Landau level at the charge neutral Dirac point splits into four sub-levels, lifting both sublattice and spin degeneracy. The QH effect at $\nu = \pm 4$ is investigated in tilted magnetic field and can be attributed to lifting spin-degeneracy of the $n = \pm 1$ Landau level.

4.1 Landau Level Splitting in Graphene

The experiment is performed in Nation High Magnetic Field Laboratory (NHMFL) in Tallahassee, Florida. The sample is measured in a ^{3}He cryostat. A total magnetic field up to 45 T can be generated using a combination of superconducting and resistive magnet. A rotator stage allows for 180° continuous rotaion in the magnetic field. The magneto-resistance (R_{xx}) and Hall resistance (R_{xy}) of the graphene sample are measured using Lock-in amplifiers at an excitation current of 10 nA.

Figure 4.1 displays R_{xx} and R_{xy} measured simultaneously as a function of V_g at $B = 45$ T and at a temperature of $T = 1.4$ K. A series of fully developed QH states, i.e., zeros in R_{xx} and plateaus in R_{xy} quantized to values $h/e^2\nu$ with an integer filling factor ν, are observed. Well-defined $\nu = \pm 2$ QH states and a $\nu = -6$ state are visible in these traces, in accordance with the previous low-magnetic field measurement ($B < 9$ T)[8, 37]. In addition to these QH states, new QH states at $\nu = \pm 1$ and ± 4 are clearly resolved in the high magnetic field data.

We also note that both R_{xx} and R_{xy} fluctuate but remain at finite values (of the order of 100 kΩ, see Fig. 4.1 right inset) near the Dirac point where the carrier density is low. The detailed traces of R_{xx} and R_{xy} vary near the Dirac point for different gate sweeps in magnetic field $B > 25$ T. We speculate that this irreproducibility is caused by the detailed trapped charge configuration in the gate dielectric, whose Coulomb potential is not screened due to the low carrier density in graphene near the Dirac point.

In order to investigate the development of the new QH states in high magnetic fields, we carried out magneto-transport measurements in various magnetic fields between 9 T and 45 T at $T = 1.4$ K. The Hall conductivity, σ_{xy}, deduced from R_{xx} and R_{xy} using formula $\sigma_{xy} = R_{xy}/(R_{xy}^2 + W^2 R_{xx}^2/L^2)$, is plotted as a function of V_g in

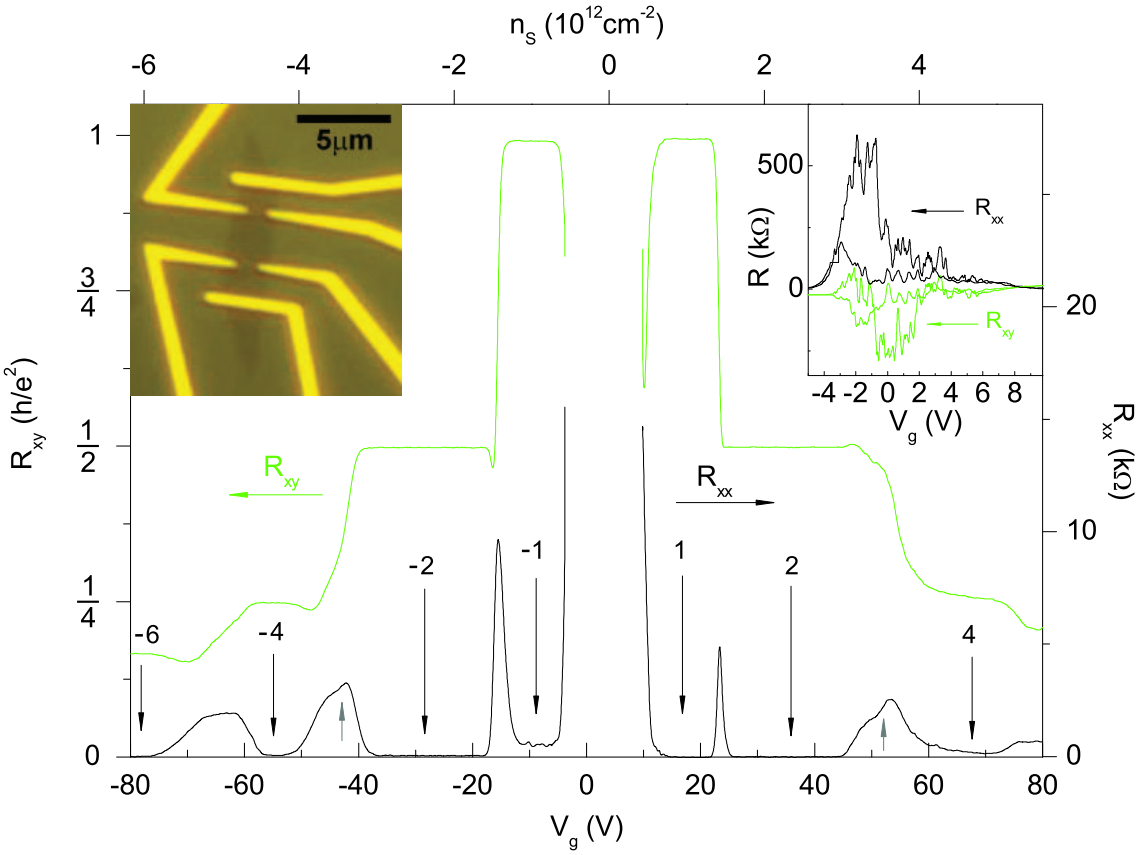

Figure 4.1: R_{xx} and R_{xy} measured in the device shown in the left inset, as a function of V_g at $B = 45$ T and $T = 1.4$ K. $-R_{xy}$ is plotted for $V_g > 0$. The numbers with the vertical arrows indicate the corresponding filling factor ν. Gray arrows indicate developing quantum Hall states at $\nu = \pm 3$. n_s is the sheet carrier density derived from the geometrical consideration. Right inset: R_{xx} (dark solid lines) and R_{xy} (light solid lines) for another device measured at $B = 30$ T and $T = 1.4$ K in the region close to the Dirac point. The two sets of data are taken at different times under the same conditions. Left inset: an optical microscope image of a graphene device used in this experiment.

Fig. 4.2. Here, W and L are the width and length of the channel between the voltage probes respectively. In addition to the QH plateaus at $\nu = \pm 4(|n| + 1/2)$ observed in lower magnetic field ($B < 9$ T), new QH plateaus appear at higher magnetic fields. Specifically, $\nu = 0$ QH plateau is resolved at $B > 11$ T, and $\nu = \pm 1, \pm 4$ plateaus start to appear at similar field $B \sim 17$ T. The fact that the $\nu = \pm 1$ and ± 4 plateaus are resolved at similar magnetic fields suggests that the LL splitting responsible for these QH states may have the same origin.

The $\nu = 0$ QH plateau right at the Dirac point ($V_g \approx 3.7$ V) is intriguing. While σ_{xy} exhibits a clearly resolved $\nu = 0$ plateau for $B > 11$ T (Fig. 4.2), R_{xx} shows a finite peak ($R_{xx} \sim 40$ kΩ as $R_{xy} \to 0$ at $B = 25$ T, see Fig. 4.2, upper inset). This new type of QH state does not conform to the standard QH observation (i.e., zeros in R_{xx}), and certainly deserves further study.

The new set of QH states, $\nu = 0, \pm 1$ and ± 4, are only observed at high magnetic fields. They can be attributed to the magnetic field induced splitting of the $n = 0$ and $n = 1$ LLs. In lower B-fields, each LL at energy E_n is assumed to be four-fold degenerate due to a two-fold spin degeneracy and a two-fold sublattice symmetry (i.e. $\mathbf{K}$ and $\mathbf{K}'$ degeneracy)[16]. The observed filling factor sequence $\nu = 0$ ($B > 11$ T) and $\nu = \pm 1$ ($B > 17$ T) implies that the degeneracy of $n = 0$ is fully lifted in high magnetic fields, such that σ_{xy} increases in steps of e^2/h as the Fermi energy passes through the Landau Levels (LLs), whose substructure is now resolved. While the $n = 0$ LL is totally resolved into $\nu = 0, \pm 1$ plateaus, the four-fold degeneracy in the $n = \pm 1$ LLs is only partially resolved into $\nu = \pm 4$, leaving a two-fold degeneracy in each of these LLs. Although a close examination of R_{xx} and R_{xy} hints at developing QH states corresponding to $\nu = 3$ (Fig. 4.1, gray arrows), their relatively weaker features strongly indicate that there exists a hierarchy of degeneracy lifting in these

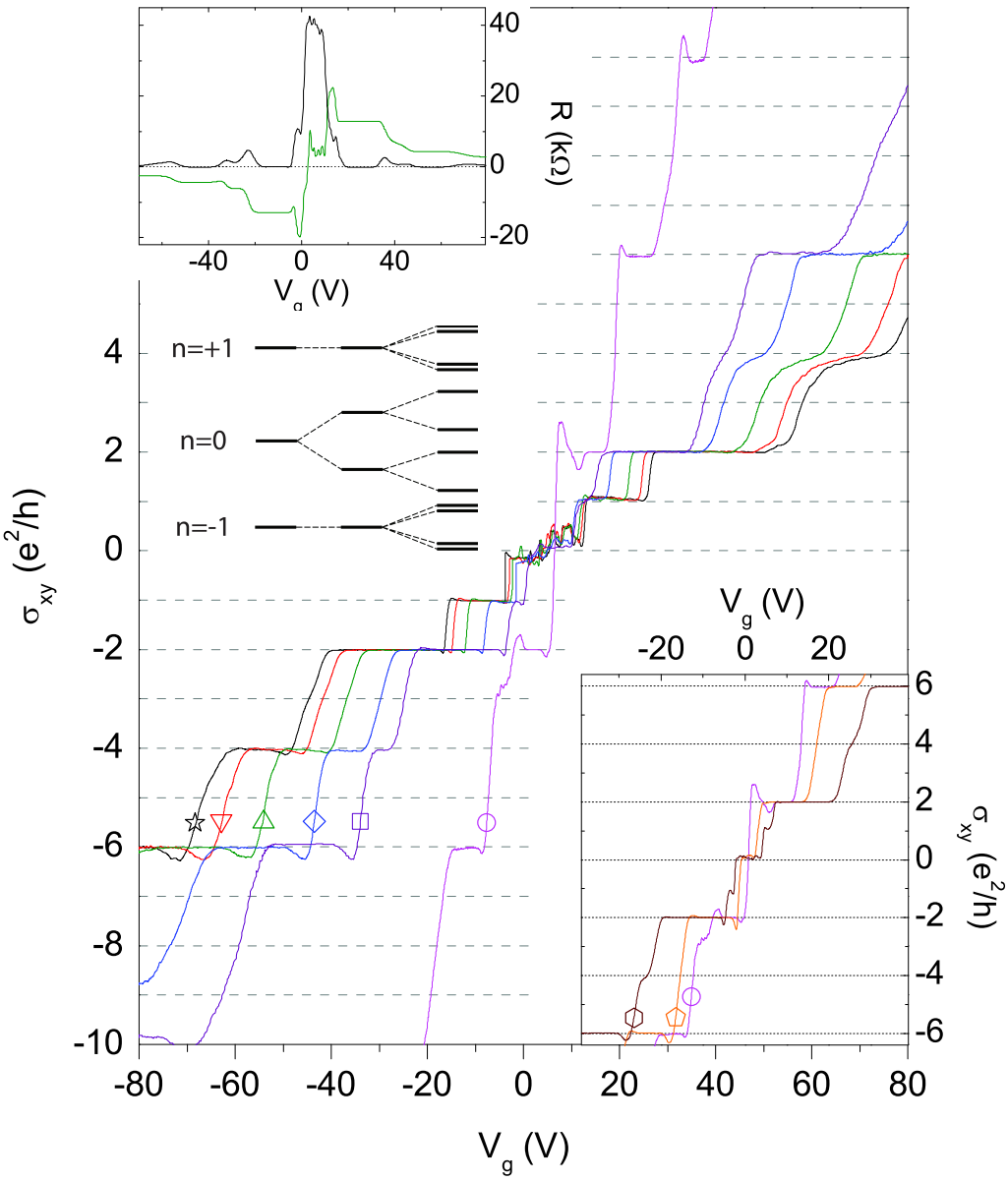

Figure 4.2: σ_{xy}, as a function of V_g at different magnetic fields: 9 T (circle), 25 T (square), 30 T (diamond), 37 T (up triangle), 42 T (down triangle), and 45 T (star). All the data sets are taken at $T = 1.4$ K, except for the $B = 9$ T curve, which is taken at $T = 30$ mK. Left upper inset: R_{xx} and R_{xy} for the same device measured at $B = 25$ T. Left lower inset: a schematic drawing of the LLs in low (left) and high (right) magnetic field. Right inset: detailed data near the Dirac point for B = 9 T (circle), 11.5 T (pentagon) and 17.5 T (hexagon).

LLs, as shown schematically in the lower inset of Fig. 4.2.

We can map out the sequence of the LL splitting when the magnetic field increases. The $\nu = 0$ state appears at a rather low field ($B \approx 11$ T). Then comes $\nu = \pm 1$ and $\nu = \pm 4$ states at about the same field ($B \approx 17$). The fact that $\nu = \pm 1$ and $\nu = \pm 4$ start to develop at the same field suggests that they may have the same origin. Since $\nu = \pm 4$ has been found to originate from spin-splitting, so $\nu = \pm 1$ is very likely due to spin-splitting, too. Armed with this knowledge, we speculate that $\nu = 0$ is from the sublattice splitting.

Considering that the presence of a magnetic field alone does not break the inversion symmetry of graphene lattice, the broken sublattice symmetry in graphene in high magnetic fields is rather surprising. The observed LL splitting bears a resemblance to the valley degeneracy splitting observed in the 2D electron gas in Si inversion layers [4] and AlAs quantum wells [38], where the lifting of the valley degeneracy occurs due to uniaxial strain or due to a many-body induced correlation effect such as "valley skyrmions"[39]. Since the sublattice symmetry is protected by inversion symmetry in graphene, simple uniaxial strain does not lift the graphene sublattice degeneracy. This leaves many-body electron correlation within the LL as a possible origin for the lifting of the degeneracy at the Dirac point. We point out that a high magnetic field anomaly has been observed in bulk graphite[40], possibly originating from the formation of a charge density wave (CDW) due to Fermi surface nesting of the electron and hole LLs. In addition, a recent theoretical study suggests that CDW order may open up a gap at the Dirac point in high magnetic fields [41], further substantiating the possibility of a many-body origin of our observation of fully lifted LL degeneracies. We also note that very recent theoretical studies suggest other many body effects [42, 43].

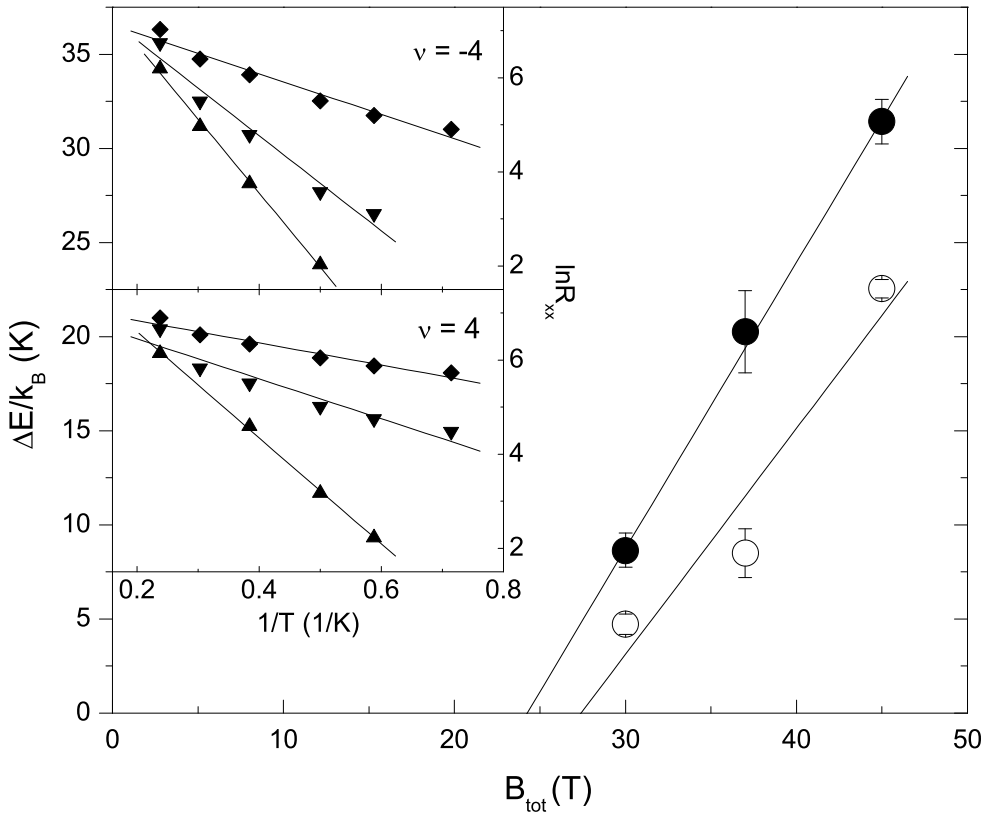

Figure 4.3: Inset: R_{xx}^{min} at $\nu = -4$ (upper inset) and $\nu = +4$ (lower inset) for $B_{tot} = 30$ T (diamond), 37 T (down triangle) and 45 T (up triangle), applied to normal to graphene plane. The straight lines are linear fits to the data. The main figure: the activation energy, ΔE, as a function of B_{tot} for filling factor $\nu = -4$ (filled circle) and $\nu = +4$ (open circle). The straight lines are linear fits to the data.

4.2 The $\nu = 4$ Quantum Hall State

We now turn our attention to $\nu = \pm 4$ QHE states and study the origin of the lifting of this degeneracy in the $n = \pm 1$ LLs. We determine the energy gap, ΔE, between LLs by measuring the temperature dependence of the associated R_{xx} minimum, R_{xx}^{min}. The inset of Fig. 4.3 shows Arrhenius plots of R_{xx}^{min} which reveal thermally activated behavior, $R_{xx}^{min} \sim \exp(\Delta E/2k_BT)$ (k_B is the Boltzmann constant). We find that ΔE,

derived from linear fits to these data depends linearly on total magnetic field, B_{tot}, applied normal to the graphene plane, as shown in the main section of Fig. 4.3. The energy gap at $\nu = \pm 4$ could be the result of two possible scenarios: (i) Spin splitting whose energy scales as $\Delta E_S = g^* \mu_B B_{tot}$, where g^* is the effective g-factor and μ_B is the Bohr magneton; or alternatively, (ii) sublattice symmetry breaking and gap formation due to many-body correlations. In order to distinguish these two different mechanisms, we performed transport measurements in a tilted magnetic field. Since the electron system in graphene is only 3 Å thick, a total magnetic field, B_{tot}, applied at tilt angle, θ, with respect to the direction normal to the graphene plane (Fig. 4.4a inset) affects in-plane motion relevant to electron-electron correlation only via the perpendicular field $B_p = B_{tot} \cos(\theta)$. The electron spin, on the other hand, experiences the full B_{tot}, and hence spin splitting is independent of θ. Fig. 4.4a shows the minima in R_{xx} corresponding to the $\nu = -4$ QH state at identical B_p but different B_{tot}: $B_{tot} = 30$ T ($\theta = 0°$) and $B_{tot} = 45$ T ($\theta = 49.0°$). At fixed B_p, R_{xx}^{min} depends on B_{tot}. This strongly suggests that $\nu = -4$ originates from spin splitting of the LL but not from any in-plane electron correlation. Following this argument, the energy gap of these spin-split LLs can now be written as [4]:

$$\Delta E = \Delta E_S - 2\Gamma \tag{4.1}$$

where Γ is the half-width of the LL broadening at half maximum. Assuming that Γ is a constant, then g^* and Γ can be extracted from the slope and y-intercept of linear fit: $g^* = 2.0$ and $\Gamma = 18.2$ K are obtained from Fig. 4.3 for $\nu = -4$ QH state and $g^* = 1.7$ and $\Gamma = 15.8$ K for $\nu = 4$ QH state from a similar analysis (not shown). The fact that these measured g-factors are very close to that of the bare electron ($g^* = 2$) further substantiates the spin-splitting origin of the $\nu = \pm 4$ QH states. We also note

that these Γ values are in good agreement with the estimation, $\hbar/\tau$, where $\tau = 100$ fs is the relaxation time deduced from the carrier mobility in the zero magnetic field limit.

Finally, we discuss our measurement of R_{xx} at $\nu = \pm 4$ at $T = 1.4$ K in a tilted magnetic field. Here we kept B_{tot} fixed at 45 T, and varied θ to change B_p. As shown in Fig. 4.4b, the minima display pronounced changes as θ increases, seemingly contradicting our previous conclusion that $\nu = -4$ QH state originates from spin polarized LLs whose energy level separation (ΔE_S) only depends on B_{tot}. This contradiction is resolved if we relax our previous assumption regarding a constant Γ, and take into account the B_p dependence of the Landau level width $\Gamma(B_p)$. Indeed, a phenomenological linear relation for $\Gamma(B_p)$ can be obtained from the exponential dependence of R_{xx}^{min} on B_p (inset to Fig. 4.4b). From the linear fit (solid line in the inset to Fig. 4.4b), we obtain $\Gamma(B_p) = \Gamma_0 - 0.14B_p$ up to a constant, Γ_0, the LL broadening at the zero field limit. Here Γ_0 is in the unit of Kelvin and B_p is in Tesla. Combining this functional form of $\Gamma(B_p)$ with Eq. 4.1, the experimentally observed linear relation of $\Delta E(B_{tot} = B_p)$ (Fig. 4.3) now yields slightly reduced g-factors: $g^* = 1.8$ for $\nu = -4$ and $g^* = 1.4$ for $\nu = +4$.

4.3 Conclusion and Discussions

In conclusion, we observe the splitting of LLs under high magnetic field up to 45 T. We discover that the $n = 0$ LL splits into four sublevels, lifting both spin and sublattice degeneracy, potentially indicating a many-body correlation in this LL.

In the $n = \pm 1$ LL, only two-fold degeneracy seems to be lifted within experimentally accessible high magnetic field, leaving the sublevels still two-fold degenerate.

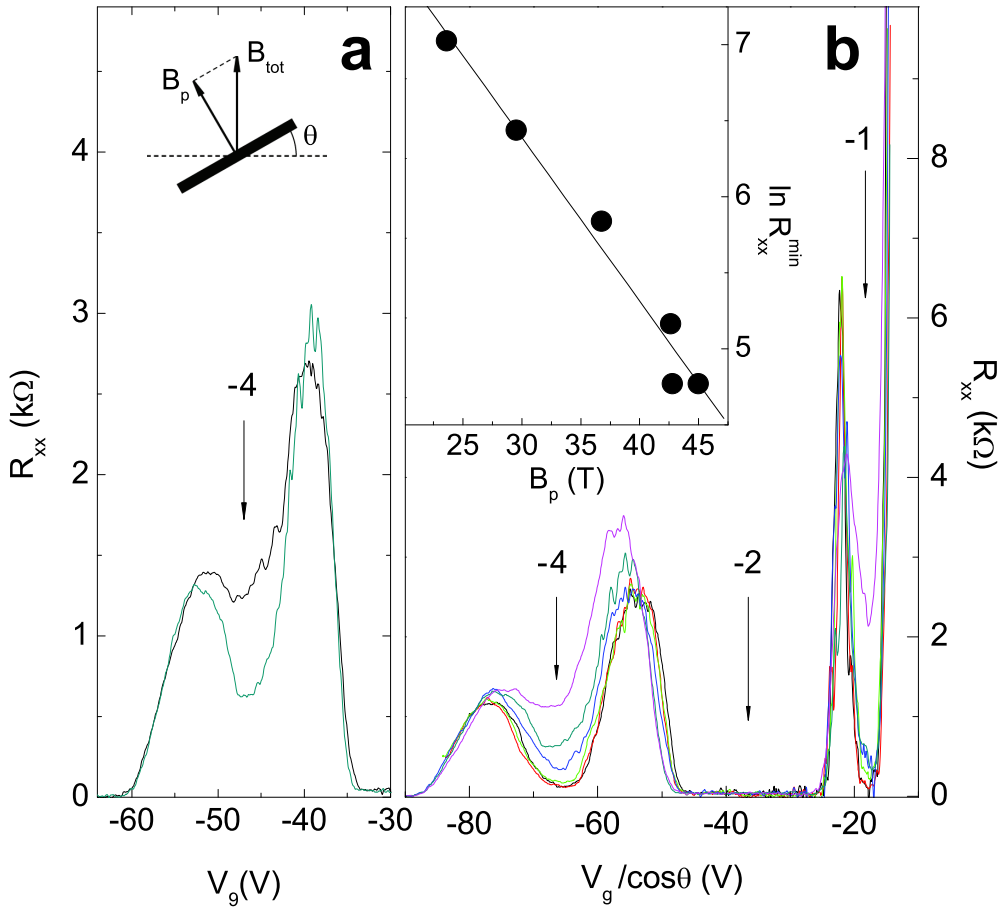

Figure 4.4: (a) R_{xx} measured as a function of gate voltage around $\nu = -4$ at $B_p = 30$ T at two different total magnetic fields, $B_{tot} = 45$ T (light solid line) and $B_{tot} = 30$ T (dark solid line). Numbers with vertical arrow indicates filling factors. Inset: a schematic drawing of the measurement configuration. (b) R_{xx} measured as a function of V_g. Data are taken at $B_{tot} = 45$ T at six different tilt angles: $0°, 18.1°, 18.8°, 35.5°, 49.0°, 58.4°$ (ascending order from bottom at $\nu = -4$). Inset: R_{xx}^{min} at $\nu = -4$ plotted on natural logarithmic scale as a function of B_p. The straight line is a linear fit to the data.

Measurements at $\nu = -4$ indicate that the splitting is function of the total magnetic field, when the perpendicular field is fixed. This observation strongly suggests that $\nu = \pm 4$ QH state originates from spin-splitting. The effective g-factors are determined by the linear dependence of the energy gap at $\nu = \pm 4$ on the total magnetic field and they are found to be close to the bare electron g-factor.

Chapter 5

Multilayer Graphene

5.1 Background – Band Structure of Graphite

Graphite is a three-dimensional crystal, in which graphene layers are stacked in the ABAB sequence with van der Waals interactions. The resulting hexagonal lattice, shown in Fig. 5.1, has each successive layer displaced horizontally so that half of the carbon atoms (full circles) are immediately above (or under) atoms in the neighboring layers and the other half (open circles) are exactly above (or under) centers of hexagons. The in-plane bonding length is the same as that in graphene, $a_0 = 1.42$ Å, and the distance between the neighboring layers is $c_0 = 3.35$ Å. In an rectangular coordinates (x, y, z), the three fundamental translation vectors are

$$\mathbf{a_1} = a(1/2, \sqrt{3}/2) \qquad \mathbf{a_2} = a(-1/2, \sqrt{3}/2) \qquad \mathbf{a_3} = c(1, 0, 0) \tag{5.1}$$

as indicated in Fig. 5.1. The in-plane lattice constant is $a = \sqrt{3}a_0 = 2.46$ Å, and the out-of-plane lattice constant is double the spacing between two adjacent layers,

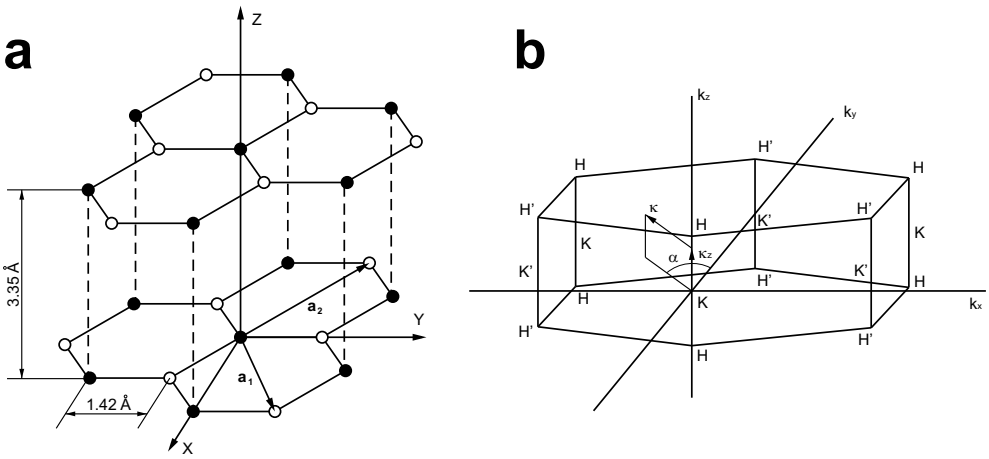

Figure 5.1: The crystal structure (a) and Brillouin zone (b) of graphite.

$c = 2c_0 = 6.71$ Å. The translation vector in graphite lattice can thus be defined as $\mathbf{R} = n_1\mathbf{a_1} + n_2\mathbf{a_2} + n_3\mathbf{a_3}$, where n_1, n_2, and n_3 are integers. The translation vectors $\mathbf{a_1}$, $\mathbf{a_2}$, and $\mathbf{a_3}$ correspond to a reciprocal lattice with the following basis vectors:

$$\mathbf{b_1} = \frac{4\pi}{\sqrt{3}a}(\sqrt{3}/2, 1/2) \qquad \mathbf{b_2} = \frac{4\pi}{\sqrt{3}a}(-\sqrt{3}/2, 1/2) \qquad \mathbf{b_3} = \frac{2\pi}{c}(0, 0, 1) \tag{5.2}$$

The first Brillouin zone for the hexagonal lattice of graphite is a hexagonal prism, shown in Fig. 5.1. The corners are $\mathbf{H}, \mathbf{H'}$, and the centers of the side edges are $\mathbf{K}, \mathbf{K'}$.

In addition to the hexagonal lattice described above, another less frequent form of graphite is a rhombohedral lattice. The in-plane lattice parameters and inter-layer spacing remain the same for the rhombohedral graphite. It only differs from the hexagonal graphite in that the graphene layers are stacked in the sequence ABCABC, instead of ABAB. In a rhombohedral lattice, the center of a carbon hexagon in the A layer is directly below a corner of a hexagon in the B layer, which is in turn directly below an inequivalent corner of a hexagon in the C layer. The influence of various layer stacking in graphite has been investigated by Haering (1958) [44], McClure

(1969) [45], Samuelson et al. (1980) [46]. They have shown that different types of stacking significantly modifies the band structure, especially around the Fermi level.

Bulk graphite has been the subject of extensive theoretical and experimental studies since 1950s. A generally accepted energy band model, commonly referred to as the SWMC-model, has been developed by Slonzewski, Weiss and McClure in 1960s. SWMC-model concentrates only on the energy states in the vicinity of the vertical edges of the Brillouin zone **HKH** and $\mathbf{H'K'H'}$, where the electron and hole Fermi surfaces reside. The variation of energy along the zone edge is found by a rapidly convergent Fourier expansion. In the basal plane, the energy dependence on wavevector $\boldsymbol{\kappa} = (\kappa_x, \kappa_y)$, measured from the zone edge, is found by using $\mathbf{k} \cdot \mathbf{p}$ perturbation theory, taking zero-order wave-function as those at the vertical edge HKH of the Brillouin zone. In essence, the SWMC-model extends the linear dispersion relation in graphene to the three-dimensional case in graphite, using the $k \cdot p$ method. A complete description of the Fermi surface requires seven parameters, which are determined by experimental data. Fig. 5.2 displays the Fermi surface along one of the Brillouin zone edges. There are three majority pockets, two of which are at the corner (**H**) containing holes and one of which is in the center (**K**) containing electrons.

It is worth noting that the designation of electron and hole pockets was reversed in the literature published before 1968. That mistake was subsequently corrected through the effort of Schroeder et al. (1968), McClure (1970), Mrozowski (1971), and Toy et al. (1977). An electron pocket at the center of Brillouin zone edge is also found consistent with our experimental results.

Various degrees of approximations have been utilized in the past based on SWMC-model. Here we briefly discuss the Simple Two-band (STB) model [47], which which has been successful in explaining electron transport in bulk graphite [48, 49]. The

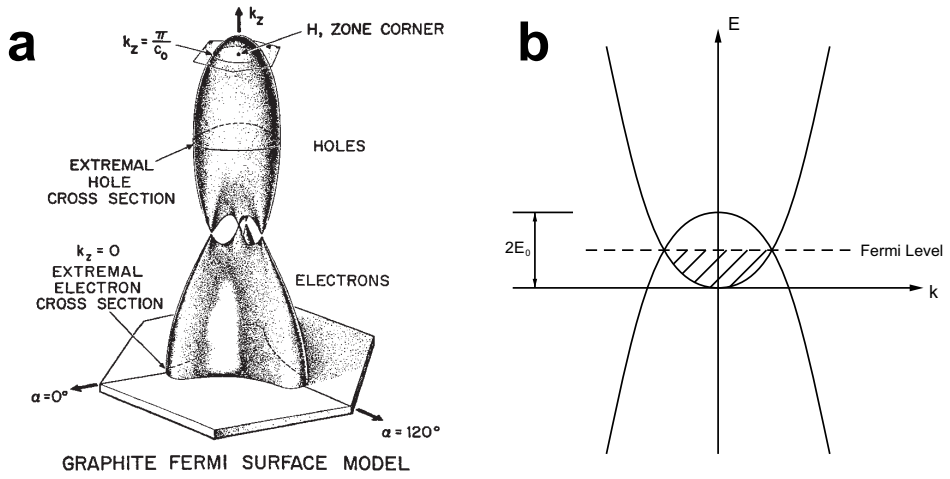

Figure 5.2: Energy band structure of graphite. Left: Fermi surface model of graphite (M. S. Dresselhaus et al., 1964). The electron pocket is located at **K** and hole pocket is located at **H**. Right: A simple two-band model of the energy band structure of graphite. The electron and hole pockets are simplified as parabolic bands with a overlap energy E_0.

STB model neglects, in the first order approximation, the energy variation along the edges of the Brillouin zone, and approximates the Fermi surfaces in graphite with cylinders. This approximation results in a parabolic two-band system described by

$$E_e = \frac{\hbar^2 \kappa^2}{2m_e^*} \tag{5.3}$$

$$E_h = 2E_0 - \frac{\hbar^2 \kappa^2}{2m_h^*} \tag{5.4}$$

Here e and h refer to the electrons and holes. m_e^* and m_h^* denote the effective mass of electrons and holes, respectively. $2E_0$ is the energy overlap between electron band and hole band, and $\kappa = |\boldsymbol{\kappa}|$ is the horizontal distance from the nearest Brillouin zone edge (see Fig. 5.1). In the framework of STB model, familiar concepts such as carrier densities (n_e, n_h), and mobilities (μ_e, μ_h) can be readily recovered to account for the electronic transport in graphite.

In this chapter, we present results from the electronic transport measurement in mesoscopic graphite crystallites with thicknesses ranging from 12 nm to 90 nm. The samples are fabricated using the "Nano-pencil" method described in section 2.2. The mesoscopic nature of such samples allows us to tune the Fermi level continuously, utilizing a back gate electrode. This is a unique experimental advantage only present in mesoscopic samples, as previous experiments have demonstrated that gate electric field has little effect in bulk graphite [50].

The conduction through such graphite crystallites as a function of gate electric field and temperature without the presence of external magnetic field will be described in section 5.2. In the following section 5.3, we report galvanomagnetic transport, which is strongly modulated by the gate electric field, in magnetic fields up to 9 Tesla. Electric field effect (EFE) dependent Shubnikov de Hass (SdH) oscillations, signatures of Landau level formation of electrons and holes, have been observed at low temperatures. In addition, the effective mass of electrons and holes are measured by investigating the temperature damping of SdH amplitudes for each type of carrier.

5.2 Electric-Field-Dependent Conduction

Fig. 5.3 shows the conductance, G, versus the gate voltage, V_g, at temperature $T = 1.7$ K for samples with varying thicknesses. The curves are normalized with their minimum values $G_{min} = G(V_g^{min})$, where $V_g^{min} \approx -40$ V. As $\Delta V_g = V_g - V_g^{min}$ moves away from zero, $G(V_g)$ increases, increasing more rapidly for thinner samples. Specifically, at $\Delta V_g = 100$ V, G/G_{min} is 1.47 and 1.12 for the samples with thickness 12 and 42 nm respectively, while no appreciable change is observed in the 95 nm sample. This observation implies a larger electric field effect in thinner samples, as

expected.

Considering the electrostatic coupling between the samples and the gate, the observed behavior of $G(V_g)$ at low temperatures can be understood quantitatively as discussed below. When the gate voltage is applied, the electrostatic potential at the surface of the sample rises to ϕ_0, and a charge density $n_{ind}(z)$ is induced in the sample, where z is measured from the interface of the sample and the substrate. Following the Thomas-Fermi approximation, the electrostatic potential in the sample is given by $\phi(z) = \phi_0 e^{-z/\lambda_s}$, where ϕ_0 is a constant (determined below) and λ_s is the screening length. λ_s can be inferred from $\phi/\lambda_s^2 = -en_{ind}/\varepsilon_0$, where e and ε_0 are the electron charge and vacuum permittivity, respectively. The total amount of induced charge in the sample with thickness d is related to the capacitance of the sample to gate per unit area, C_g, by $C_g(V_g - \phi_0) = -\int_0^d en_{ind}(z)dz$. By evaluating this integral, we obtain $\phi_0 = V_g/(1 + C_Q/Cg)$, where the sample dependent quantum capacitance per unit area is $C_Q = \varepsilon_0(1 - e^{-d/\lambda_s})/\lambda_s$.

In order to estimate the enhanced conductance in the presence of an induced charge density gradient, we use Einstein's relation for local conductivity $\sigma(z) = e^2 N(E_F)D(E_F)$, where $N(E_F)$ and $D(E_F)$ are the density of states and the electron diffusion coefficient at Fermi energy E_F, respectively. In graphite both of these quantities are sensitive to changes in E_F, thus it should be accounted for in the determination of local conductivity in the presence of an electric field. Assuming our samples retain the band structure of bulk graphite, the functional form of $N(\epsilon)$ can be obtained from graphite band structure calculations (Fig. 5.3 inset) [1, 51]. Here ϵ is measured from the charge neutral point, where $N(\epsilon)$ has its minimum value. For the energy range $|\epsilon| < 300$ meV, we can approximate $N(\epsilon) \approx N_0(1 + \beta|\epsilon|)$, where $N_0 = 5.2\times10^{20}$ cm^{-3}eV^{-1} and $\beta = 4.8$ ev^{-1}. A further assumption is required to

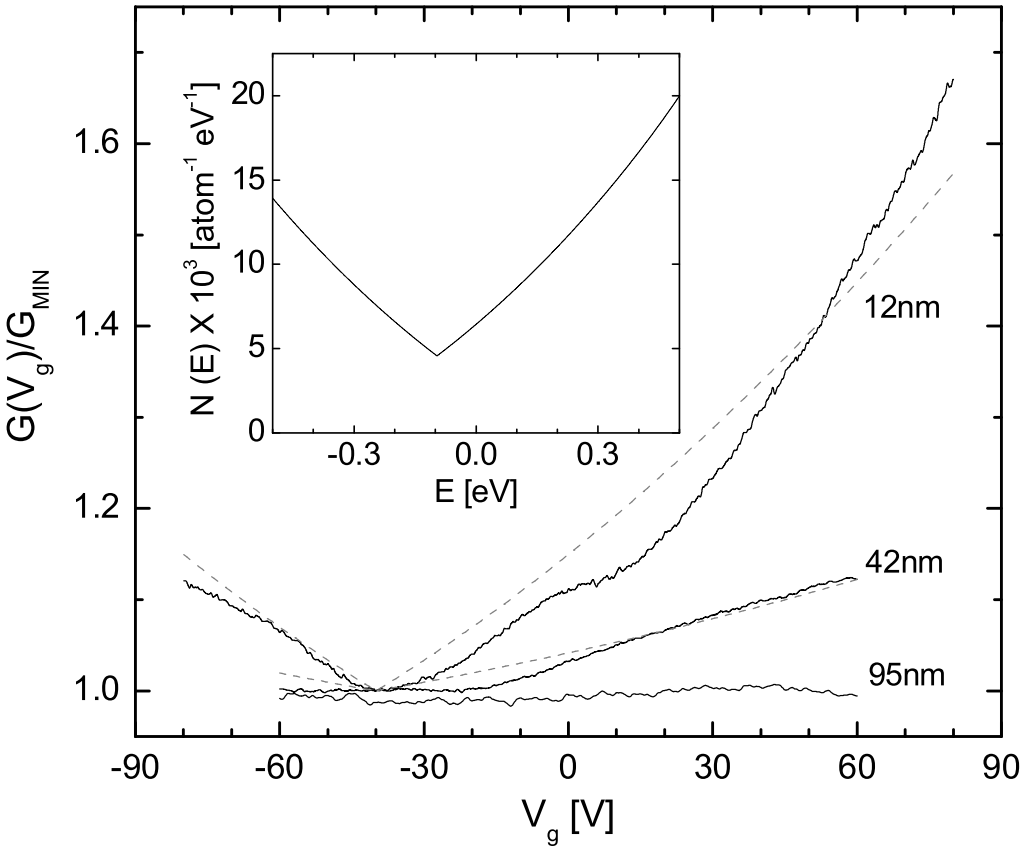

Figure 5.3: Gate electric field modulation of conductance of mesoscopic graphite sample. Conductance (normalized to its minimum value) is measured in samples of varying thickness as a function of gate voltage at T =1.7 K. The broken lines are the fit to a model. Inset: Calculated density of states for bulk graphite.

estimate $D(E_F)$ in the presence of an electrostatic potential. Here we adopt the STB model. Assuming the scattering time, τ, and effective mass of carriers are relatively insensitive to change of E_F, the STB model yields $D(\epsilon) \propto v_F^2 \tau \propto |\epsilon + E_0|$, where v_F is the Fermi velocity and E_0 half the band overlap between the electron and hole bands. With these assumptions, the normalized conductance of the sample is given by

$$G(V_g)/G_{min} = \int_0^d dz N(\epsilon)|\epsilon + E_0|/N_0 E_0 d \tag{5.5}$$

where $\epsilon(z) = -e\phi_0 e^{-z/\lambda_s}$. In order to compare this equation to our experimental observations, the values of λ_s and E_0 are needed. We use $\lambda_s = 0.4$ nm, a value obtained from the literature [52], and $E_0 = 16$ meV and 19 meV for the 12 nm and 42 nm samples respectively, which are obtained from temperature dependent resistance measurement discussed below. Employing these values, we estimate C_g by comparing Eq. (5.5) to the experimentally observed values (Fig. 5.3). The estimated C_g are 36 aFμm^{-2} and 30 aFμm^{-2} for the 12 nm and 42 nm thick graphite devices, respectively. Assuming a parallel plate capacitance model, the geometrical considerations yield capacitance value 75 aFμm^{-2} for our devices. The factor of two difference between these values most probably originates from the partial electrostatic screening by the contacts [53].

We now turn our attention to the temperature dependence of the electrical conductance in samples with varying thickness. Fig. 5.4 shows the resistivity normalized to its room temperature value, $\rho(T)/\rho(300K)$, as a function of temperature, T, for d ranging from 12 – 95 nm at $V_g = 0$. While the thicker samples show a metallic behavior ($d\rho/dT > 0$), thinner samples develop a more complicated behavior in T. This behavior can be understood by considering two competing factors as the temperature varies. Assuming the mobility, μ, is similar for the compensating electrons and holes

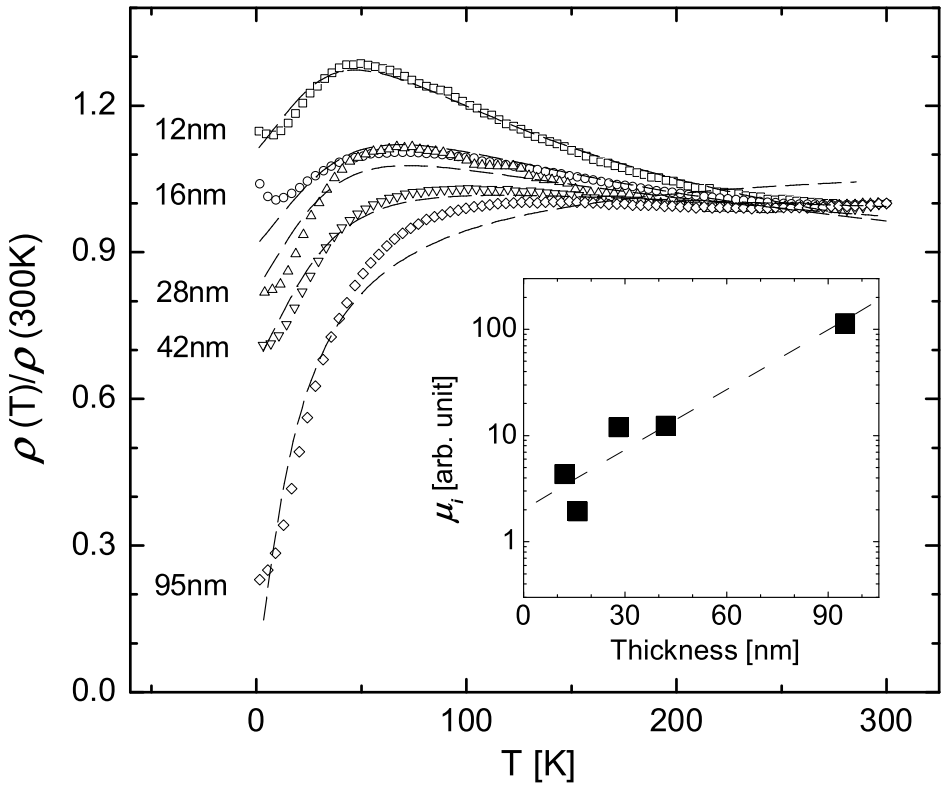

Figure 5.4: Resistivity (normalized to its 300 K value) as a function of temperature for different thicknesses. Broken lines are fits with the STB model. Inset: The mobility due to static disorder, as a result of fits to the STB model. The dotted line is an empirical fit.

in the samples, the sample resistivity is given by $\rho = 1/(|e|\mu n)$, with the total charge carrier density $n = n_e + n_h$, where n_e and n_h are the carrier densities of electrons and holes, respectively. In the STB model, for completely compensated samples (i.e., $\Delta V_g = 0$), $n/2 = n_e = n_h = C_0 k_B T \ln\left(1 + \exp\frac{E_0}{k_B T}\right)$, where k_B is Boltzmann constant and C_0 a constant independent of T [54]. We further assume that the mobility can be expressed as $\mu^{-1} = \mu_i^{-1} + A_0 T$, where μ_i^{-1} is the contribution from static scattering centers and A_0 is a constant depending on electron-phonon scattering in graphite. Then, as T increases, μ decreases due to increasing electron-phonon scattering, while n increases rapidly due to the thermal excitation of charge carriers around E_F. Using E_0 and $A_0\mu_i$ as fitting parameters, this model fits well with our experimental observations over a large temperature range and samples with varying thicknesses (broken lines in Fig. 5.4). As a result of the fit, we obtain $E_0 \sim$ 10 - 20 meV, which is in reasonable agreement with the values found in the literature [55]. In addition, we obtain $A_0\mu_i$ from the same fit. The constant A_0, which strongly depends on the electron-phonon interaction strength in graphite, is less sensitive to the change of d than μ_i. Assuming A_0 is similar for all measured samples, the μ_i for different samples can be compared. The inset of Fig. 5.4 suggests a tendency of decreasing μ_i as sample thickness is reduced. Therefore, these measurements provide an evidence that boundary scattering is stronger in thinner samples. We note, however, that the zero thickness extrapolation of μ_i is finite. In addition, our galvanomagnetic measurements in these samples, discussed in the next section, showed that the quantum oscillations in electron transport can be readily observed at high magnetic fields. Both observations suggest that the quality of the sample has not degraded significantly after our micromechanical extraction from the bulk.

5.3 Galvanomagnetic Properties

Fig. 5.5 displays the Hall resistance (R_{xy}) and the MR (R_{xx}) as a function of applied magnetic field, B, measured in a 12 nm thick graphite sample at temperature $T = 1.7$ K. The excitation current is kept at 0.5 μA for both R_{xy} and R_{xx} measurements. The magnetic field is applied perpendicularly to the graphite basal plane. Both quantities exhibit oscillatory features on top of smooth backgrounds as B varies. Near $V_g \approx 0$ V, the MR and Hall resistance exhibit similar behavior to that observed in high quality bulk graphite [56]: The positive MR background is ascribed to the general nature of magnetotransport in materials with coexisting nearly compensated electron and hole carriers [57], while the oscillations on top of the background are related to the Shubnikov de Haas (SdH) effect, the quantum oscillations due to Landau level formation [12]. Remarkably, as we vary the gate voltage, V_g, the behavior of R_{xx} and R_{xy} changes dramatically. The background in the MR is most prominent at $V_g^{max} \approx -15$ V. As V_g moves away from this value, the slope of the MR background becomes much smaller. The change of Hall measurement is even more drastic: $R_{xy}(B)$ changes its sign of overall slope as $\Delta V_g = V_g - V_g^{max}$ swings from negative to positive values, indicating that ΔV_g changes the dominant majority charge carriers from holes to electrons. This is a somewhat surprising result at first sight, since the thickness of the sample (12 nm) is still an order of magnitude larger than the screening length of graphite ($\lambda_s \approx 0.4$ nm [52]), and thus only a relatively small portion of the sample is affected by the gate electric field. We will discuss this point quantitatively below.

The aforementioned electric field effect (EFE) in mesoscopic graphite samples is clearly presented by observing R_{xx} as a function of gate voltage at a fixed magnetic field. Fig. 5.6 shows R_{xx} as a function of V_g at a large magnetic field ($B_m = 8.5$ T) for two samples ($d = 12$ and 42 nm). As expected from Fig. 5.5, R_{xx} has a peak near a

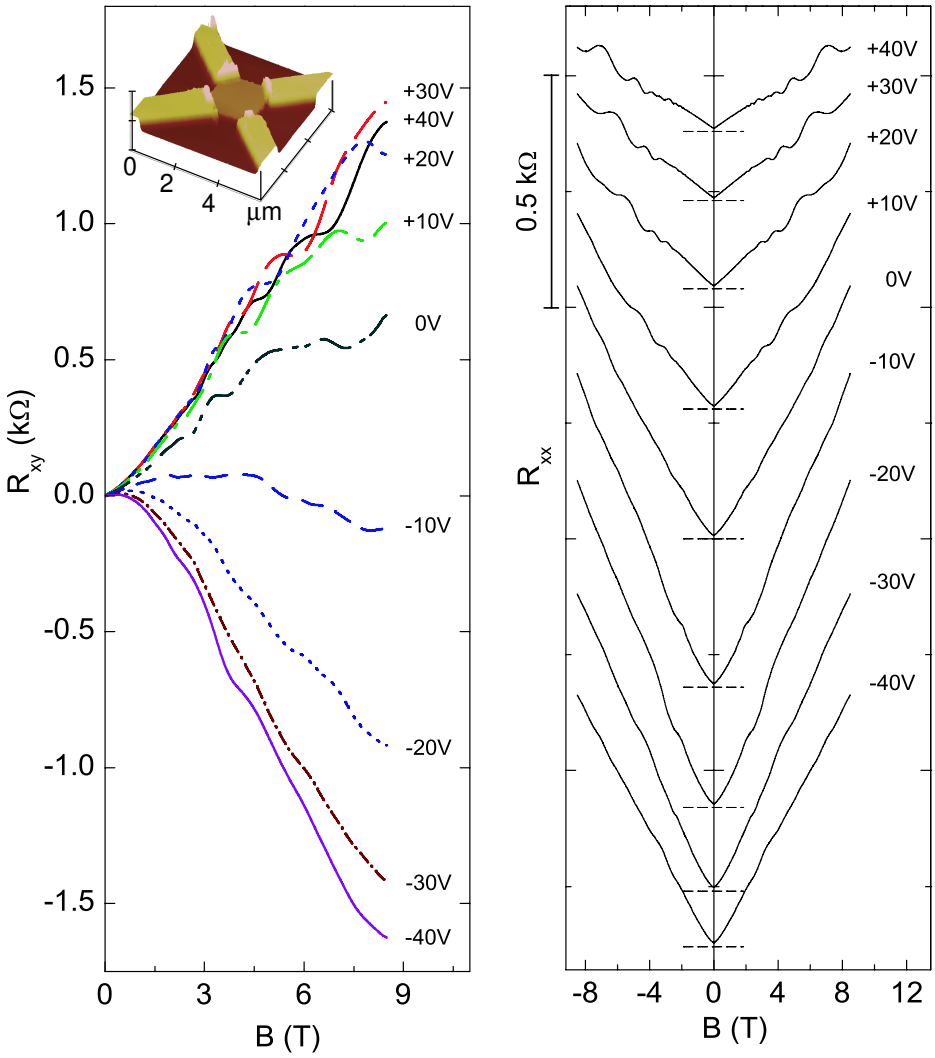

Figure 5.5: Gate electric field modulation of galvanomagnetic transport in mesoscopic graphite. The inset shows an AFM image of a 12 nm thick mesoscopic graphite sample with four electrodes at the corners for galvanomagnetic measurements. The left and right panel show the Hall resistance (R_{xy}) and magneto-resistance (R_{xx}) respectively as a function of magnetic field measured at $T = 1.7$ K in this device. Numbers near each curve indicate the applied gate voltages. In the right panel, curves are shifted for clarity and the dashed lines correspond to the zero lines of each curve.

gate voltage where $\Delta V_g \approx 0$, falling slowly as $|\Delta V_g|$ becomes large. We found that this gate dependence strongly depends on d. For the 12 nm sample, R_{xx} is suppressed to $\sim 10\%$ of its peak value, while it is still $\sim 60\%$ for the 42 nm sample at $\Delta V_g = 80$ V. Such a sensitive dependence of $R_{xx}(V_g)|_{B_m}$ on d is indicative of the reduced EFE by screening of induced charge near the sample surface.

We measured 6 mesoscopic graphite samples with thicknesses ranging from 12 - 95 nm. Similar results were found samples with similar geometries. It was found, however, that V_g^{max} is slightly different from sample to sample and also depends on sample preparation history.

In order to elucidate the dependence of R_{xx} on V_g, we employ the STB model. The STB model assumes that the bottom of the electron band and the top of the hole band overlap with a small band overlap $2E_0$ near the Fermi energy E_F. The resistivity of a sample, ρ, in the presence of a magnetic field can be expressed by [12, 57]:

$$\frac{\Delta\rho}{\rho_0} = \frac{4\mu^2 B^2 n_e n_h/(n_e+n_h)^2}{1+[\mu B(n_e-n_h)/(n_e+n_h)]^2} \tag{5.6}$$

where $\rho_0 = \rho(B=0)$, $\Delta\rho = \rho(B) - \rho_0$, μ is the average carrier mobility, and n_e and n_h are the carrier concentrations of electrons and holes, respectively. Generally, $\Delta\rho$ varies the most as a function of B when electrons and holes are nearly compensated (i.e., $n_e \approx n_h$). From Fig. 5.6, we infer that this condition is met at $V_g \approx V_g^{max}$ where the growth of the MR background as a function of B is strongest in our samples (see the curves for $V_g = -10$ V and $V_g = -20$ V in Fig. 5.5). As ΔV_g increases from zero, the induced charge in the sample screens the gate electric field and the electrostatic potential in the sample is given by $\phi(z) = \phi_0 e^{-z/\lambda_s}$, where z is measured from the interface between the sample and the substrate. The constant ϕ_0 can be determined from the electrostatic gate coupling to the sample. By integrating over

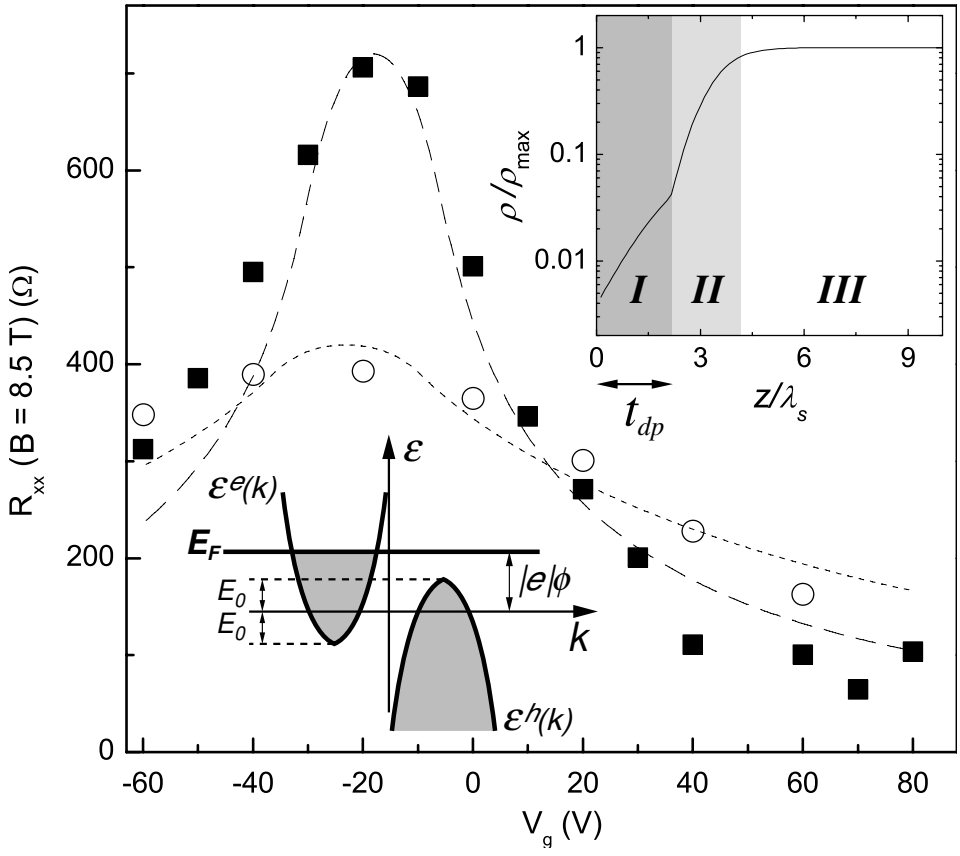

Figure 5.6: Magneto-resistance measured in 12 nm (solid square) and 42 nm (open circle) thick sample at various gate voltages. The dashed and dotted lines are fits to a model described in text. The lower inset shows a schematic STB diagram for electron ($\varepsilon^e(k)$) and hole ($\varepsilon^h(k)$) in the presence of electrostatic potential induced by the gate. The electron band and hole band are displaced in k for a better view. Upper inset represents the local magneto-resistivity across the sample, assuming $\phi_0 = 8E_0/|e|$ as an example. Symbols are defined in text.

the induced charge in the sample, we obtain $\phi_0 = \alpha \Delta V_g$ with the constant $\alpha^{-1} = 1 + \varepsilon_0(1 - e^{-d/\lambda_s})/\lambda_s C_g$, where C_g is the gate capacitance per unit area of the sample and ε_0 is the vacuum permittivity.

We incorporate this local electrostatic potential to the STB model by considering a gradient in n_e and n_h. Suppose $\Delta V_g > 0$, the local electrostatic potential will pull down the electron and hole bands by $|e|\phi(z)$ (Fig. 5.6 lower inset). For a sufficiently large gate voltage, such that $|e|\phi_0 > E_0$, the sample can be divided into three regions by introducing a hole depletion depth, $t_{dp} = \lambda_s \log(|e|\phi_0/E_0)$: (I) $0 < z < t_{dp}$, where $n_h \simeq 0$; (II) $t_{dp} < z \lesssim t_{dp} + \lambda_s$, where $0 < n_h < n_e$; and (III) $z > t_{dp} + \lambda_s$, where $n_h \approx n_e$. In region (I), only electrons participate in the transport, and $\rho(z)$ increases as z approaches zero, owing to the electric field induced accumulation of n_e near the surface. In region (II), the MR is described by Eq. 5.6, so a steep increase of $\rho(z)$ is expected as $n_e - n_h$ becomes small. In region (III), the gate electric field is completely screened, so $n_e \approx n_h$ and $\rho(z) \approx \rho_{max} = R_{xx}(\Delta V_g = 0)d$. The exact opposite argument works for a sufficiently large negative gate voltage, where electrons are depleted. Note that for small $|\Delta V_g|$, where $|e\phi_0| < E_0$, region (I) disappears (i.e., $t_{dp} = 0$). From the above discussion, we now build a quantitative model to describe $\rho(z)$. According to the STB model $n_e(\epsilon)$, $n_h(\epsilon) \propto \epsilon^{3/2}$, where ϵ is measured from the bottom of the respective band edge, and $\rho(z)/\rho_{max}$ is obtained from Eq. 5.6 (Fig. 5.6 upper inset). Then the resistance of the sample can be evaluated from $R_{xx}^{-1} = \int_0^d \rho^{-1}(z)dz$ for fixed B and V_g. Following in this way, a reasonable fit is obtained for both the 12 nm (dashed line) and 42 nm (dotted line) samples as shown in Fig. 5.6. In this fit, we use $E_0 = 15$ meV, a value quoted in [55], and obtain $C_g = 26$ aF/μm^2 (12 nm sample) and 24 aF/μm^2 (42 nm sample) as a result of the fit. These capacitance values are in reasonable agreement with our previous estimates using different analysis on the same samples in section 5.2. It is noteworthy that for

a large V_g such that $|e|\phi_0 \gg E_0$, $\rho(z) \ll \rho_{max}$ in region (I), and thus a significant portion of the total current flows in this region. Furthermore, as ΔV_g increases, t_{dp} grows only logarithmically. Even at $\Delta V_g \approx 100$ V, the largest gate voltage applied, $t_{dp} \approx 1$ nm, which corresponds to only ~ 3 bottom layers. Therefore, only a few of the bottom layers of the sample are responsible for the observed EFE modulation of the galvanomagnetic transport quantities.

We now turn our attention to the quantum oscillations observed in our mesoscopic graphite samples. The strong EFE modulation of the carrier density in the bottom layers allows us to probe the quantum oscillations in these layers with a continuously tunable carrier concentration. Fig. 5.7(a) redisplays the separated SdH oscillations as a function of B^{-1}, obtained from the MR data shown in Fig. 5.5 after subtracting out the smooth background. The SdH oscillations indicate the oscillatory density of states at E_F as a quantized Landau level passes through E_F. The frequency of SdH oscillations, f_s, is related to the extremal area of the electron and hole pockets of the Fermi surface by $f_s = \hbar c A_k^{e,h}/2\pi|e|$, where A_k^e and A_k^h are the areas of extremal electron and hole pockets [12]. Since n_e and n_h are modulated by V_g, the observed variation of f_s can be explained by the change of $A_k^{e,h}$.

In order to demonstrate the change of f_s quantitatively, we first locate the major peaks (solid symbols) and valleys (open symbols) in the SdH oscillations after low pass filtering of the data. The value of B^{-1} for a peak (valley), B_m^{-1}, is indexed by ν, an integer (a half integer) number that corresponds to the Landau level responsible for the particular oscillation. Fig. 5.7(b) shows that each set of points (B_m^{-1}, ν) at a given V_g are on a straight line that intercepts the origin, implying that the period of the SdH oscillations is regular. From the slope of these lines we obtain f_s at different V_g (Fig. 5.7(b) inset). The obtained f_s's are increasing with $|\Delta V_g|$. Therefore, we believe

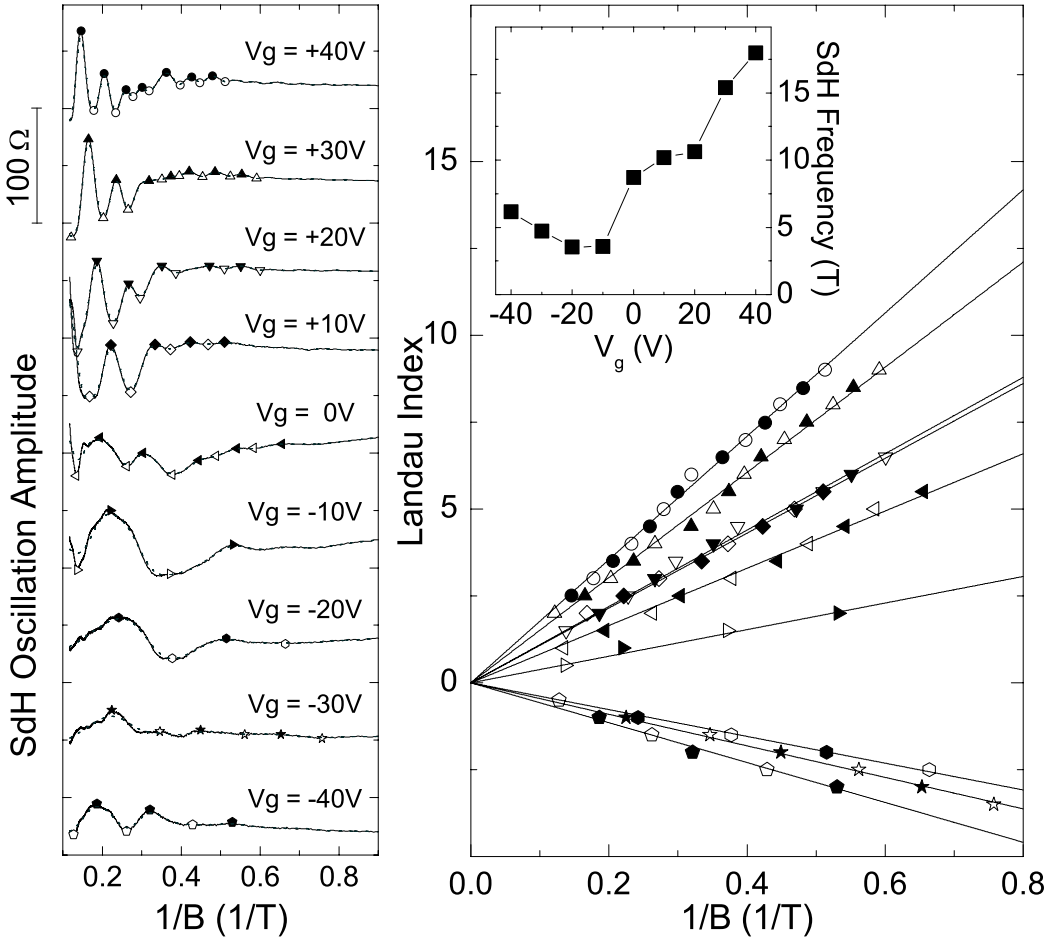

Figure 5.7: (a) The SdH Oscillations observed in Fig. 5.5, after subtraction of smooth backgrounds. Solid (open) symbols correspond to peak (valley) of the oscillations found after passing the curve through a low pass filter (dotted line). Curves are displaced for clarity. (b) Landau plots (see text) obtained from (a). Negative indices are assigned to the hole branch for clarity. Lines are linear fits to each set of points at different V_g. Inset: the frequency of the SdH oscillations obtained from the slopes of the line fits in (b) as a function of gate voltage.

that the obtained f_s corresponds to A_k^e for $\Delta V_g > 0$ and to A_k^h for $\Delta V_g < 0$. This conclusion allows us to compare the experimentally observed f_s with the expected value from the STB model. Assuming the Fermi surface of graphite is described by the overlap of electron and hole bands in the STB model, $A_k^e \propto (\alpha \Delta V_g + E_0)$ and $A_k^h \propto (-\alpha \Delta V_g + E_0)$. This relationship leads to $f_s(|\Delta V_g|)/f_s^0 = 1 + \alpha |\Delta V_g|/E_0$, where $f_s^0 = f_s(\Delta V_g = 0)$. From the values of α and E_0, determined separately above, we estimate $f(\Delta V_g = 50V)/f_0 \approx 4.8$, which is in reasonable agreement with the experimentally observed ratio 4.3.

Finally, we discuss the temperature dependence of the SdH oscillations. Fig. 5.8 shows the oscillatory MR at two extreme gate voltages, $V_g = +40$ V and $V_g = -60$ V, at various temperatures. At these extreme gate voltages, the transport in the sample is dominated by only one type of carrier in a few bottom layers. Thus, the SdH oscillations in the upper (lower) panel of the figure correspond to electron (hole) Landau levels in the sample. In both cases, the observed SdH oscillation amplitude is gradually damped away as the temperature increases. The temperature dependent SdH oscillation amplitude has been used to extract the effective mass of the charge carriers [13]. At a fixed magnetic field, the temperature damping factor of the SdH oscillation amplitude is given by:

$$R_T = \frac{2\pi^2 k_B T m^* / e\hbar B}{\sinh(2\pi^2 k_B T m^* / e\hbar B)} \tag{5.7}$$

where m^* is the effective mass of the carriers. We find that Eq. 5.7 fits the observed amplitude damping very well (Fig. 5.8 insets). As a result from the fittings, the effective electron mass $m_e^* = (0.052 \pm 0.002) m_e$ and hole mass $m_h^* = (0.038 \pm 0.002) m_e$ are obtained, where m_e is the bare electron mass. These values agree well with $0.057 m_e$ and $0.039 m_e$, reported effective mass of electrons and holes in high quality

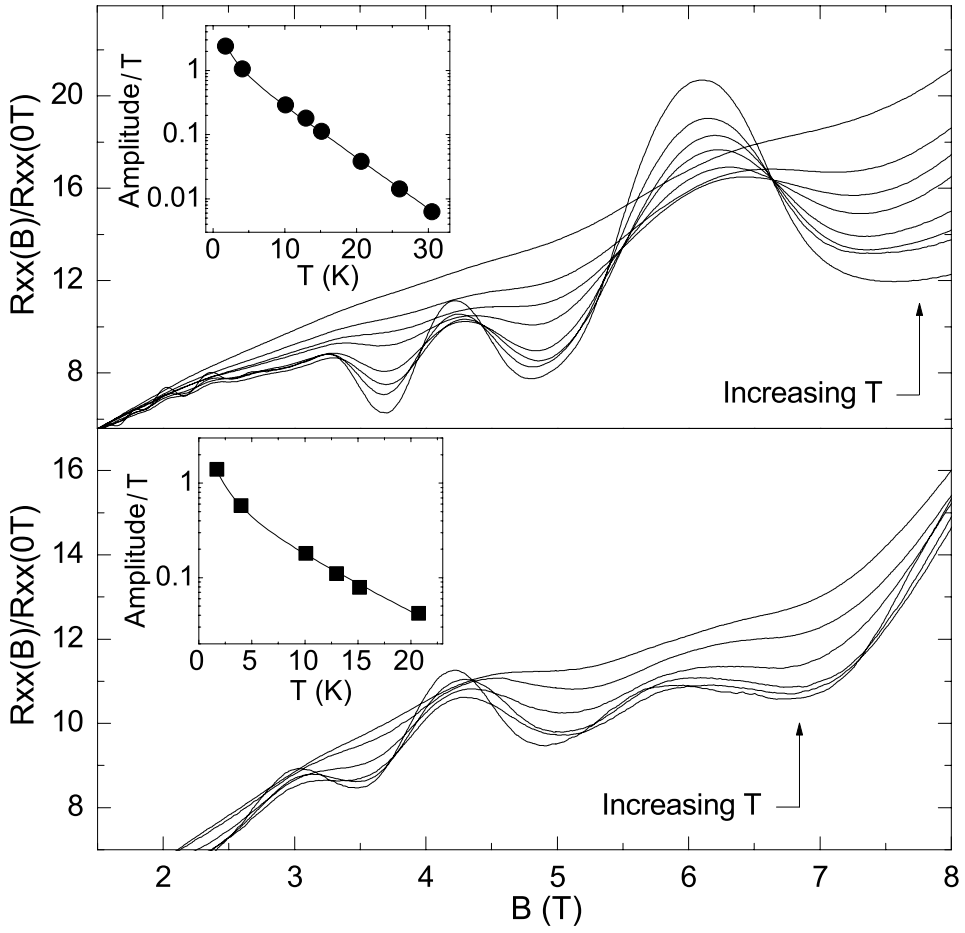

Figure 5.8: Normalized magneto-resistance of the sample in Fig 5.5 at $V_g = 40$ V (upper panel) and $V_g = -60$ V (lower panel). For the upper panel data are taken at temperatures 1.7, 4, 10, 13, 15, 20, 25, and 30 K. For the lower panel, data are taken at temperatures 1.7, 4, 10, 13, 15, and 20 K. Insets: SdH oscillation amplitudes divided by temperature, T, at a fixed magnetic field at above temperatures. The solid lines are fits to a model (see text).

bulk graphite crystal [55].

5.4 Conclusion

In summary, we have developed a unique micromechanical method to extract extremely thin graphite samples from the bulk material. Graphite crystallites with thicknesses ranging from 10 to 100 nm and lateral size similar to 2 μm are extracted from bulk. Mesoscopic graphite devices are fabricated from these samples for electric field-dependent conductance measurements. Strong conductance modulation as a function of gate voltage is observed in the thinner crystallite devices. The temperature-dependent resistivity data are analyzed in the frame work of STB model. They indicate more boundary scattering contribution in the thinner graphite samples.

Galvanomagnetic transport in those mesoscopic graphite samples are reported. Strong modulation of the Hall resistance as well as the magneto-resistance, a phenomena that was not observed before in the bulk, has been observed as the applied gate voltage changes. The Landau level formation of electron and hole carriers is also tuned by the gate. The observed phenomenon can be well described by the STB model, taking into account the carrier density gradient induced by the gate electrode. By fitting the temperature damping of the SdH oscillations, we obtain the effective carrier mass in mesoscopic graphite.

Chapter 6

Conclusions

Graphene is a novel two-dimensional system in which electron transport is governed by the relativistic quantum theory. In the past two years, graphene has arose much attention ever since its availability in isolated form. We investigate the electron transport in graphene, and discover a variety of new phenomena which stem from the effectively relativistic nature of the electron dynamics in graphene.

We have experimentally discovered an unusual Quantum Hall effect in high quality graphene samples. Different from conventional 2D systems, the observed quantization condition in graphene is described by half integer rather than integer values. The half-integer quantization, as well as the measured phase shift in magneto-oscillation, can be attributed to the peculiar topology of the graphene band structure with a linear dispersion relation and vanishing mass near the Dirac point, which is described in terms of fictitious 'relativistic' carriers. The unique behavior of electrons in this newly discovered $(2 + 1)$-dimensional quantum electrodynamics system not only opens up many interesting questions in mesoscopic transport in electronic systems with nonzero Berry's phase but may also provides the basis for novel carbon based electric and

magnetic field effect device applications, such as ballistic metallic/semiconducting graphene ribbon devices and electric field effective spin transport devices utilizing spin-polarized edge state[35].

The accessibility of high magnetic fields up to 45 Tesla allows us to study the magneto-transport in graphene in the extreme quantum limit. Under such condition, we discover new set of QH states at filling factors $\nu = 0, \pm 1, \pm 4$, indicating the lifting of the four-fold degeneracy of the previously observed QH states at $\nu = \pm 4(|n|+1/2)$, where $n$is the Landau level index. In particular, the presence of the $\nu = 0, \pm 1$ QH states indicates that the Landau level at the charge neutral Dirac point splits into four sub-levels, lifting both sublattice and spin degeneracy, potentially indicating a many-body correlation in this LL. The QH effect at $\nu = \pm 4$ is investigated in tilted magnetic field and is attributed to lifting of the $n = \pm 1$ spin-degeneracy of the Landau level.

We devote one chapter to investigation of multi-layer graphene. Strong conductance modulation as a function of gate voltage is observed in the thin crystallite devices (thickness $\sim$ 12 nm). The temperature-dependent resistivity data are analyzed in the frame work of STB model. They indicate more boundary scattering contribution in the thinner graphite samples. Galvanomagnetic transport study those samples shows strong modulation of the Hall resistance as well as the magneto-resistance, a phenomena that was not observed before in the bulk, has been observed as the applied gate voltage changes. The Landau level formation of electron and hole carriers is also tuned by the gate. The observed phenomenon can be well described by the STB model, taking into account the carrier density gradient induced by the gate electrode. By fitting the temperature damping of the SdH oscillations, we obtain the effective carrier mass in mesoscopic graphite.

Bibliography

[1] P. R. Wallace. The band theory of graphite. *Physical Review*, 71:622–634, 1947.

[2] C. Schonenberger. Bandstructure of graphene and carbon nanotubes: An exercise in condensed matter physics, 2000.

[3] J. C. Slonczewski and P. R. Weiss. Band structure of graphite. *Physical Review*, 109:272–279, 1958.

[4] T. Ando, A. B. Fowler, and F. Stern. Electronic properties of two-dimensional systems. *Reviews of Modern Physics*, 54:437–672, 1982.

[5] T. Ando, T. Nakanishi, and R. Saito. Berry's phase and absence of back scattering in carbon nanotubes. *Journal of the Physical Society of Japan*, 67:2857–2862, 1998.

[6] P. L. McEuen, M. Bockrath, D. H. Cobden, Y. G. Yoon, and S. G. Louie. Disorder, pseudospins, and backscattering in carbon nanotubes. *Physical Review Letters*, 83:5098–5101, 1999.

[7] K. S. Novoselov, D. Jiang, F. Schedin, T. J. Booth, V. V. Khotkevich, S. V. Morozov, and A. K. Geim. Two-dimensional atomic crystals. *Proceedings of the*

National Academy of Sciences of the United States of America, 102:10451–10453, 2005.

[8] Y. Zhang, Y. W. Tan, H. L. Stormer, and P. Kim. Experimental observation of the quantum hall effect and berry's phase in graphene. *Nature*, 438:201–204, 2005.

[9] Leonard I. Schiff. *Quantum mechanics*. McGraw-Hill, New York,, 3d edition, 1968.

[10] R. Jackiw. Fractional charge and zero modes for planar systems in a magnetic-field. *Physical Review D*, 29:2375–2377, 1984.

[11] F. D. M. Haldane. Model for a quantum hall-effect without landau-levels - condensed-matter realization of the parity anomaly. *Physical Review Letters*, 61:2015–2018, 1988.

[12] Neil W. Ashcroft and N. David Mermin. *Solid state physics*. Holt Rinehart and Winston, New York,, 1976.

[13] D. Shoenberg. *Magnetic oscillations in metals*. Cambridge monographs on physics. Cambridge University Press, Cambridge [Cambridgeshire] ; New York, 1984.

[14] L. M. Roth. Semiclassical theory of magnetic energy levels and magnetic susceptibility of bloch electrons. *Physical Review*, 145:434, 1966.

[15] G. P. Mikitik and Y. V. Sharlai. Manifestation of berry's phase in metal physics. *Physical Review Letters*, 82:2147–2150, 1999.

[16] S. G. Sharapov, V. P. Gusynin, and H. Beck. Magnetic oscillations in planar systems with the dirac-like spectrum of quasiparticle excitations. *Physical Review B*, 69:–, 2004.

[17] I. A. Luk'yanchuk and Y. Kopelevich. Phase analysis of quantum oscillations in graphite. *Physical Review Letters*, 93, 2004.

[18] A. Krishnan, E. Dujardin, M. M. J. Treacy, J. Hugdahl, S. Lynum, and T. W. Ebbesen. Graphitic cones and the nucleation of curved carbon surfaces. *Nature*, 388:451–454, 1997.

[19] C. Berger, Z. M. Song, T. B. Li, X. B. Li, A. Y. Ogbazghi, R. Feng, Z. T. Dai, A. N. Marchenkov, E. H. Conrad, P. N. First, and W. A. de Heer. Ultrathin epitaxial graphite: 2d electron gas properties and a route toward graphene-based nanoelectronics. *Journal of Physical Chemistry B*, 108:19912–19916, 2004.

[20] R. F. Frindt. Superconductivity in ultrathin nbse2 layers. *Physical Review Letters*, 28:299, 1972.

[21] Y. Ohashi, T. Hironaka, T. Kubo, and K. Shiiki. *Tanso*, 1997:235, 1997.

[22] X. K. Lu, H. Huang, N. Nemchuk, and R. S. Ruoff. Patterning of highly oriented pyrolytic graphite by oxygen plasma etching. *Applied Physics Letters*, 75:193–195, 1999.

[23] L. A. Girifalco and R. A. Lad. Energy of cohesion, compressibility, and the potential energy functions of the graphite system. *Journal of Chemical Physics*, 25:693–697, 1956.

[24] K. S. Novoselov, A. K. Geim, S. V. Morozov, D. Jiang, Y. Zhang, S. V. Dubonos,

I. V. Grigorieva, and A. A. Firsov. Electric field effect in atomically thin carbon films. *Science*, 306:666–669, 2004.

[25] L. X. Zheng, M. J. O'Connell, S. K. Doorn, X. Z. Liao, Y. H. Zhao, E. A. Akhadov, M. A. Hoffbauer, B. J. Roop, Q. X. Jia, R. C. Dye, D. E. Peterson, S. M. Huang, J. Liu, and Y. T. Zhu. Ultralong single-wall carbon nanotubes. *Nature Materials*, 3:673–676, 2004.

[26] K. von klitzing, G. Dorda, and M. Pepper. New method for high-accuracy determination of the fine-structure constant based on quantized hall resistance. *Physical Review Letters*, 45:494–497, 1980.

[27] Y. S. Zheng and T. Ando. Hall conductivity of a two-dimensional graphite system. *Physical Review B*, 65, 2002.

[28] V. P. Gusynin and S. G. Sharapov. Unconventional integer quantum hall effect in graphene. *Physical Review Letters*, 95:–, 2005.

[29] N. M. R. Peres, F. Guinea, and A. H. C. Neto. Electronic properties of disordered two-dimensional carbon. *Physical Review B*, 73, 2006.

[30] E. McCann and V. I. Fal'ko. Landau-level degeneracy and quantum hall effect in a graphite bilayer. *Physical Review Letters*, 96:086805, 2006.

[31] K. S. Novoselov, E. McCann, S. V. Morozov, V. I. Fal'ko, M. I. Katsnelson, U. Zeitler, D. Jiang, F. Schedin, and A. K. Geim. Unconventional quantum hall effect and berry's phase of 2 pi in bilayer graphene. *Nature Physics*, 2:177–180, 2006.

[32] Z. Fang, N. Nagaosa, K. S. Takahashi, A. Asamitsu, R. Mathieu, T. Ogasawara,

H. Yamada, M. Kawasaki, Y. Tokura, and K. Terakura. The anomalous hall effect and magnetic monopoles in momentum space. *Science*, 302:92–95, 2003.

[33] S. V. Morozov, K. S. Novoselov, F. Schedin, D. Jiang, A. A. Firsov, and A. K. Geim. Two-dimensional electron and hole gases at the surface of graphite. *Physical Review B*, 72:–, 2005.

[34] Y. Zhang, J. P. Small, M. E. S. Amori, and P. Kim. Electric field modulation of galvanomagnetic properties of mesoscopic graphite. *Physical Review Letters*, 94:–, 2005.

[35] C. L. Kane and E. J. Mele. Quantum spin hall effect in graphene. *Physical Review Letters*, 95:–, 2005.

[36] Y. Zhang, Z. Jiang, J. P. Small, M. S. Purewal, Y. W. Tan, M. Fazlollahi, J. D. Chudow, J. A. Jaszczak, H. L. Stormer, and P. Kim. Landau-level splitting in graphene in high magnetic fields. *Physical Review Letters*, 96:136806, 2006.

[37] K. S. Novoselov, A. K. Geim, S. V. Morozov, D. Jiang, M. I. Katsnelson, I. V. Grigorieva, S. V. Dubonos, and A. A. Firsov. Two-dimensional gas of massless dirac fermions in graphene. *Nature*, 438:197–200, 2005.

[38] Y. P. Shkolnikov, E. P. De Poortere, E. Tutuc, and M. Shayegan. Valley splitting of alas two-dimensional electrons in a perpendicular magnetic field. *Physical Review Letters*, 89, 2002.

[39] Y. P. Shkolnikov, S. Misra, N. C. Bishop, E. P. De Poortere, and M. Shayegan. Observation of quantum hall "valley skyrmions". *Physical Review Letters*, 95, 2005.

[40] Y. Iye and G. Dresselhaus. Non-ohmic transport in the magnetic-field-induced charge-density-wave phase of graphite. *Physical Review Letters*, 54:1182–1184, 1985.

[41] D. V. Khveshchenko. Magnetic-field-induced insulating behavior in highly oriented pyrolitic graphite. *Physical Review Letters*, 87:–, 2001.

[42] V. P. Gusynin, V. A. Miransky, S. G. Sharapov, and I. A. Shovkovy. Excitonic gap, phase transition, and quantum hall effect in graphene, 2006.

[43] J. Alicea and M. P. A. Fisher. Graphene integer quantum hall effect in the ferromagnetic and paramagnetic regimes, 2006.

[44] R. R. Haering. Band structure of rhombohedral graphite. *Canadian Journal of Physics*, 36:352–362, 1958.

[45] J. W. McClure. Electron energy band structure and electronic properties of rhombohedral graphite. *Carbon*, 7:425, 1969.

[46] L. Samuelson, I. P. Batra, and C. Roetti. Comparison of electronic-properties of various modifications of graphite. *Solid State Communications*, 33:817–820, 1980.

[47] C. A. Klein. Stb model and transport properties of pyrolytic graphites. *Journal of Applied Physics*, 35:2947, 1964.

[48] T. Tokumoto, E. Jobiliong, E. S. Choi, Y. Oshima, and J. S. Brooks. Electric and thermoelectric transport probes of metal-insulator and two-band magneto-transport behavior in graphite. *Solid State Communications*, 129:599–604, 2004.

[49] X. Du, S. W. Tsai, D. L. Maslov, and A. F. Hebard. Metal-insulator-like behavior in semimetallic bismuth and graphite. *Physical Review Letters*, 94, 2005.

[50] H. Kempa and P. Esquinazi. A field-effect-transistor from graphite: No effect of low gate fields, 2003.

[51] J. W. McClure. Band structure of graphite and dehaas-vanalphen effect. *Physical Review*, 1:612–618, 1957.

[52] P. B. Visscher and L. M. Falicov. Anisotropic electronic correlations in graphite. *Carbon*, 10:354, 1972.

[53] B. Babic, M. Iqbal, and C. Schonenberger. Ambipolar field-effect transistor on as-grown single-wall carbon nanotubes. *Nanotechnology*, 14:327–331, 2003.

[54] B. T. Kelly. *Physics of graphite.* Applied Science, London ; Englewood, N.J., 1981.

[55] N. B. Brandt, S. M. Chudinov, and Ya G. Ponomarev. *Semimetals 1. Graphite and its compounds.* Modern problems in condensed matter sciences ; v. 20. North-Holland ; Sole distributors for the USA and Canada Elsevier Science Pub. Co., Amsterdam ; New York New York, NY, 1988.

[56] D. E. Soule. Magnetic field dependence of the hall effect and magnetoresistance in graphite single crystals. *Physical Review Letters*, 1:347–347, 1958.

[57] I. L. Spain. Galvanomagnetic effects in graphite. *Carbon*, 17:209–222, 1979.